Selenology Today

ISSUE # 35, 2014

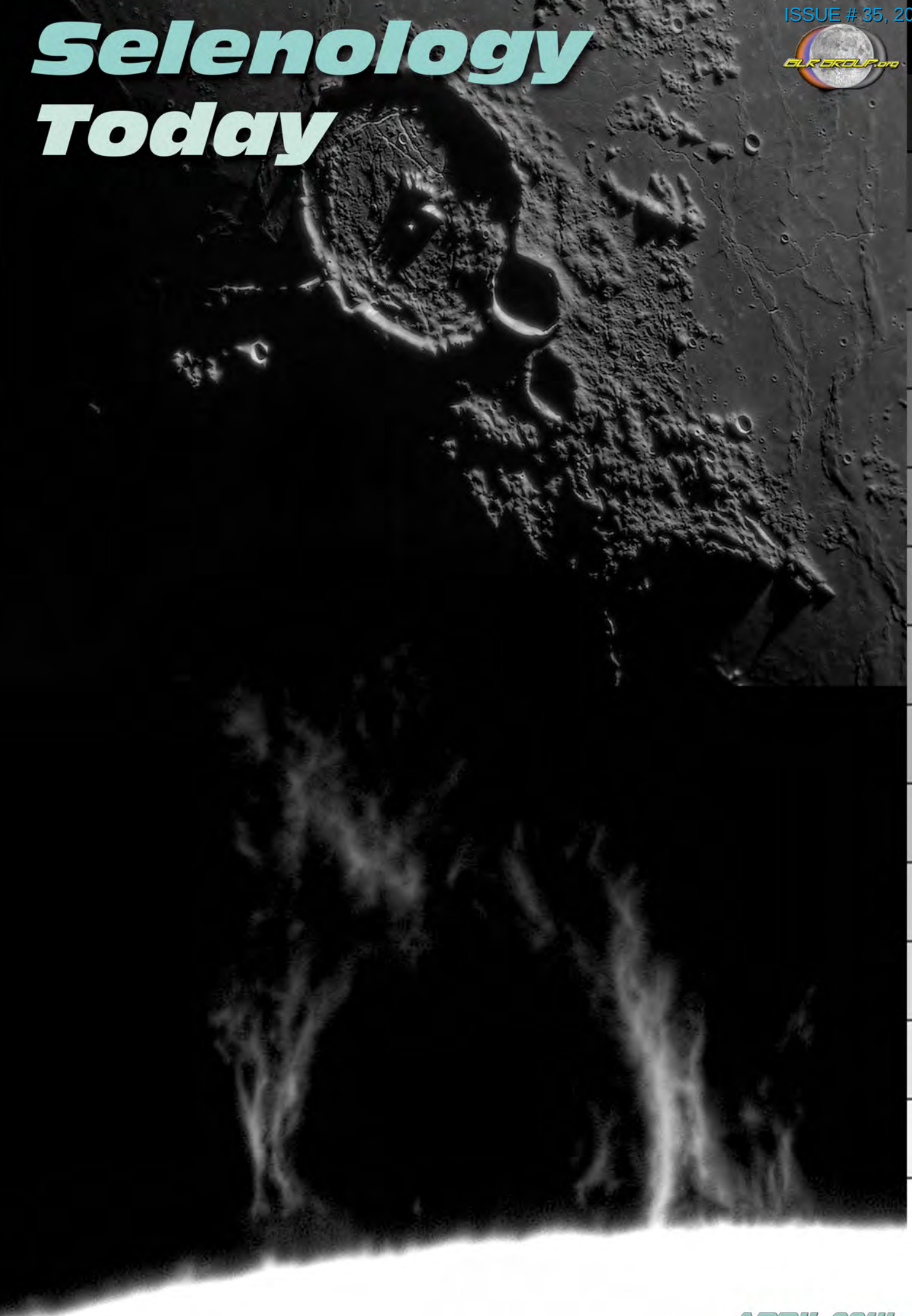

APRIL 2014

ISSUE # 35, 2014

Selenology Today

Selenology Today is devoted to the publication of contributions in the field of lunar studies. Manuscripts reporting the results of new research concerning the astronomy, geology, physics, chemistry and other scientific aspects of Earth's Moon are welcome. Selenology Today publishes papers devoted exclusively to the Moon. Reviews, historical papers and manuscripts describing observing or spacecraft instrumentation are considered.

Selenology Today website
http://digilander.libero.it/glrgroup/

and here you can found all older issues
http://www.lunar-captures.com/SelenologyToday.html

Selenology Today is under a reorganization, so that further comments sent to us will help for the new structure. So please doesn't exit to contact us for any ideas and suggestion about the Journal. Comments and suggestions can be sent to Raffaello Lena editor in chief :

gibbidomine@libero.it

ISSUE # 35, 2014

Selenology Today

Contents

COVER

- crater GASSENDI
&
Huge Solar flare

by
Mike Wirths

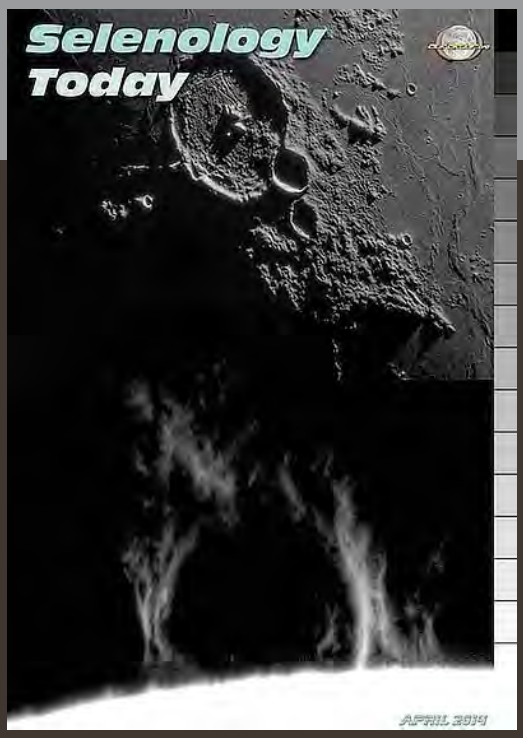

ISSUE # 35, 2014

Selenology Today

Madler – an Oblique Impact Crater

By Barry Fitz-Gerald
Geologic Lunar Research (GLR) group

Abstract

Madler is a 27km diameter crater lying on the northern rim of the Nectaris Basin. Irregular in shape, the crater exhibits an unusual distribution of ejecta which includes a bright ray extending to the south-east towards the ruined crater Daguerre. This distribution is here used to propose an oblique impact origin for the crater, and it's curious arrangement explained by the geological nature of the pre-impact site.

Madler is a somewhat irregular 27km diameter crater on the northern shore of Mare Nectaris and immediately west of the spectacular crater Theophilus. The location of the impact would appear to consist of mare plains overlain by Theophilus's ejecta blanket (Milton, 1968), but more significantly these units probably overlie submerged highland terrain which once formed the northern rim of the Nectaris Basin. These local conditions may have contributed to the irregular sub-circular shape we see, including a prominent scallop to the north where a significant wall slump has occurred. As noted by Wood (2009) this crater was originally mapped as being older than the nearby Theophilus, but he identifies features that indicate that Madler is the younger of the two. In addition, secondary craters from Madler's ejecta blanket can be detected superimposed on impact melt pools clearly associated with Theophilus, again supporting the view that Madler is the younger.

Bright ejecta from the crater is best seen telescopically, but is well represented in the Clementine imagery (Fig.1) which shows an arc of bright materiel extending approximately 1 crater radius away to the east. An asymmetric bright fan of ejecta, traceable up to 6 crater radii beyond the rim can be seen to the west of the prominent ray which extends towards Daguerre in the southwest. This light ejecta overlies secondaries from Theophilus, supporting the conclusions regarding relative crater ages, but also contains within it secondary craters from the Madler impact event. This light ejecta is more extensive to the south-west, a factor relevant to the interpretation of Madler as being the result of an oblique impact.

To the north of the crater, bright ejecta is replaced by dark ejecta which is conspicuous in the Clementine imagery (Fig.1), and can be seen extending in dark rays to the north, north-west and west across the eastern floor of Theophilus. This dark ejecta appears not to be as extensive as the bright ejecta, but this is probably a contrast effect with the brighter ejecta more conspicuous against the dark mare background. To the north-east the dark ejecta is bounded by a crater chain that extends northwards from Madler in a manner similar to the way the bright ray to the south-east forms an eastwards limit to the bright ejecta. The difference between the light and dark ejecta is most logically explained by the excavation of different source rocks by the Madler impact, with a brighter highland component of material being excavated to the south, and a more mare dominated darker material being excavated to the north. This is related to the location of the crater straddling the rim of the Nectaris Basin as discussed above.

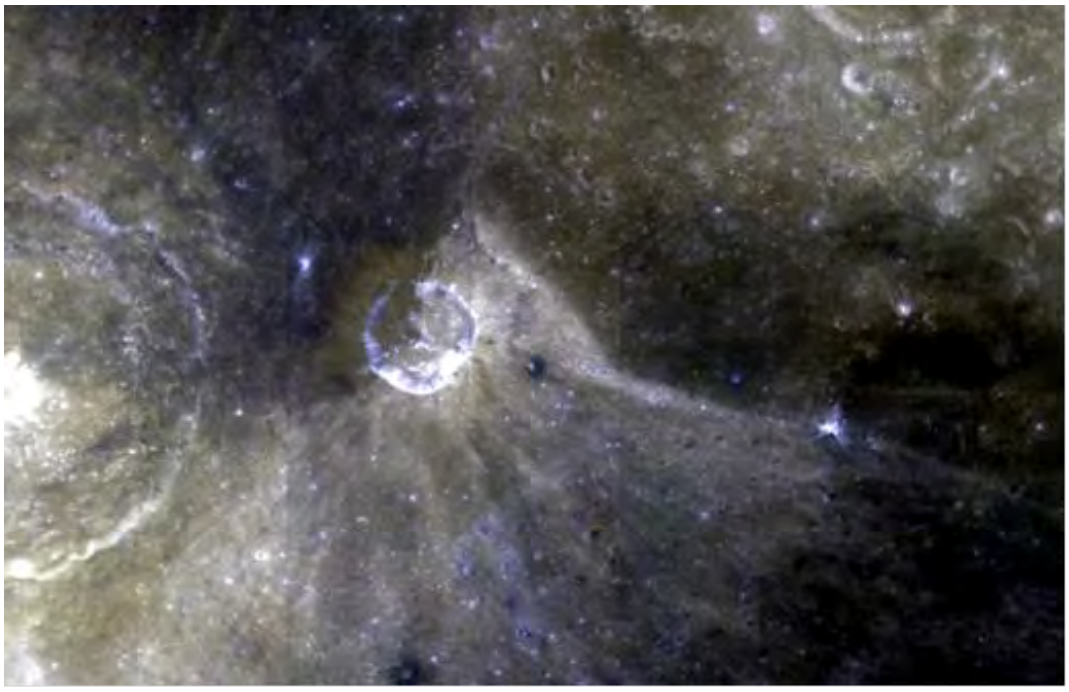

Fig.1 Clementine UVVIS Multispectral Mosaic image of Madler showing bright ray to the south-east, and light coloured ejecta to the east, south and south-west. Note bright ejecta is replaced by dark ejecta to the north.

The bright ejecta to the east of Madler forms a curious and well defined 'halo', which is bounded by the bright ray to the south-east and the crater chain to the north (Fig.2). The most distal part of this ejecta is composed of a band of almost continuous small pit like secondary craters. In some places these pits form a 'stippled' surface of individual closely spaced pits whist in other places several pits coalesce to form elongate depressions orientated tangentially to the rim of the parent crater. Eastwards of this zone the surface is sculpted by larger secondary craters presumably originating from Theophilus (Fig.3). The lack of bright ejecta eastward of the band of secondary craters, or other secondary craters obviously associated with Madler suggests a 'Zone of Avoidance' (ZoA) type of distribution, characteristic of the up-range ejecta pattern of oblique impacts.

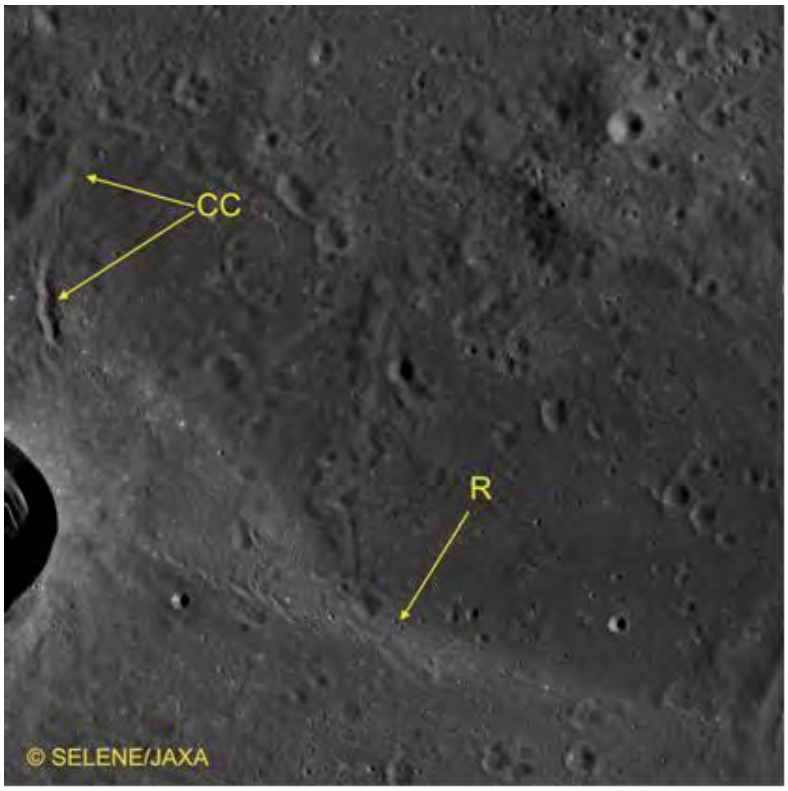

Fig.2 SELENE image of eastern side of Madler showing bright ejecta bound by crater chain to the north-east CC, and bright ray to the south-east R.

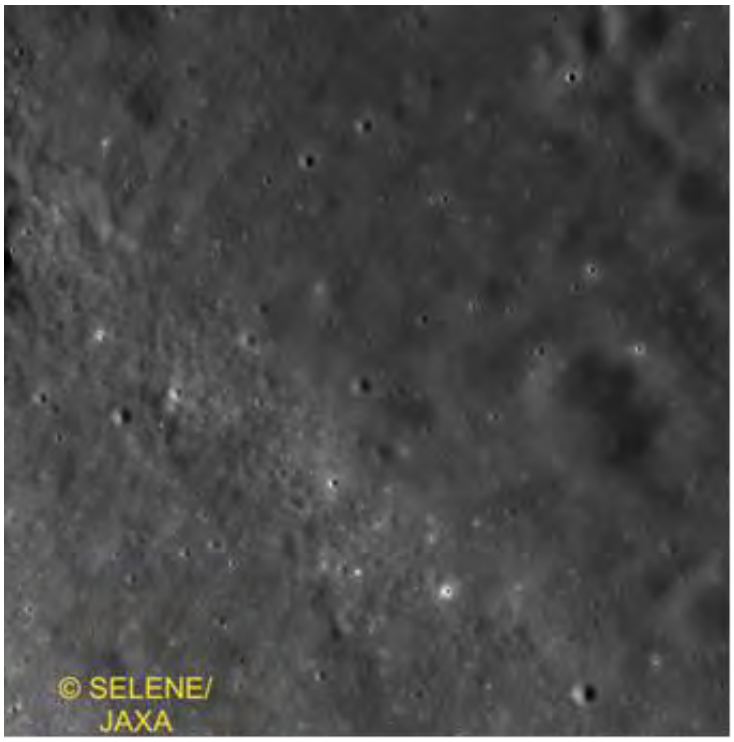

Fig.3 Detail of band of secondary crates to the east of Madler. Bright ejecta from Madler can be seen to the south-west of the band whilst to the north-east the terrain is dominated by Theophilus secondary craters.

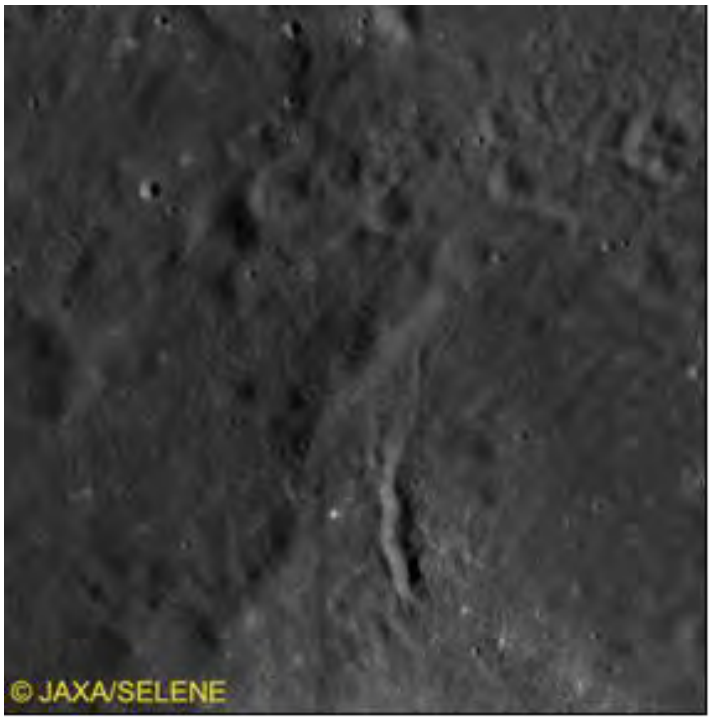

Fig.4 Detail of bright ray to the south of Madler showing en-echelon secondary craters (left) and detail of crater chain to the north showing proximal expression as an elongate depression (right).

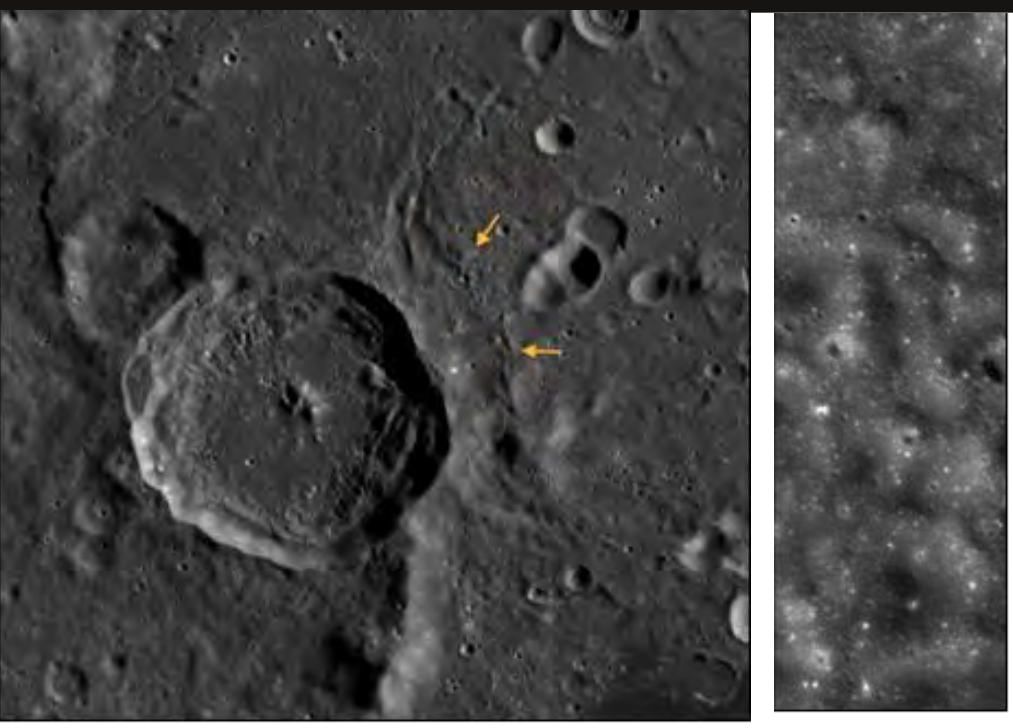

Fig.5 LRO WAC image of Dryden (left) showing arachnid ray to the north and straighter ray to the south. A narrow zone of secondary craters (yellow arrows) can be seen between them in the up-range direction. This zone can be seen to consist of elongate secondary craters and elongate ridges of ejecta orientated tangentially to the crater rim in the LROC NAC images of the same area (right).

The conspicuous ray to the south-east can be seen to have a core consisting of elongate secondary craters arranged in an en-echelon fashion (Fig.4). The crater chain to the north in contrast is not associated with a conspicuous bright ray, though a suggestion of one is visible in the Clementine images (Fig.1).

The southern ray and the northern crater chain appear to represent up-range rays which are characteristic of the up-range domain in oblique impacts. Such rays can take the form of cardioid or arachnid rays (Schultz et.al, 2009). The term 'cardioid' refers to the heart shaped appearance that results in many cases from the curvature of the rays, typically convex in an up-range direction. In the present case the southern ray exhibits little obvious curvature, whilst the northern ray if anything curves with a concave aspect up-range. Such concave up-range rays are termed 'arachnid' due to their similarity to spiders legs, and are believed to result from impacts into layered target material with a lower density surface overlying a denser basement (ibid.) Taken together, the apparent Zone of Avoidance and presence of up-range would indicate an oblique impact origin for Madler with the approach direction of the impactor being from the north-east.

The 54km diameter oblique impact crater Dryden exhibits a combination of up-range rays and a zone of secondary craters similar to those described above (Fig.5). Dryden exhibits a somewhat arachnid ray to the north, and a feinted straight ray to the south. Occupying a band between them in the up-range direction (east) is a narrow zone of secondary craters exhibiting the rather 'stippled' texture described above in relation to Madler. This zone can, on closer inspection, be seen to consist of elongate secondary craters and ejecta ridges bearing a tangential orientation to the crater rim. This indicates that these zones are a feature of oblique impacts which form in the up-range domain, possibly as result of the development and evolution of the ejecta curtain during the impact event.

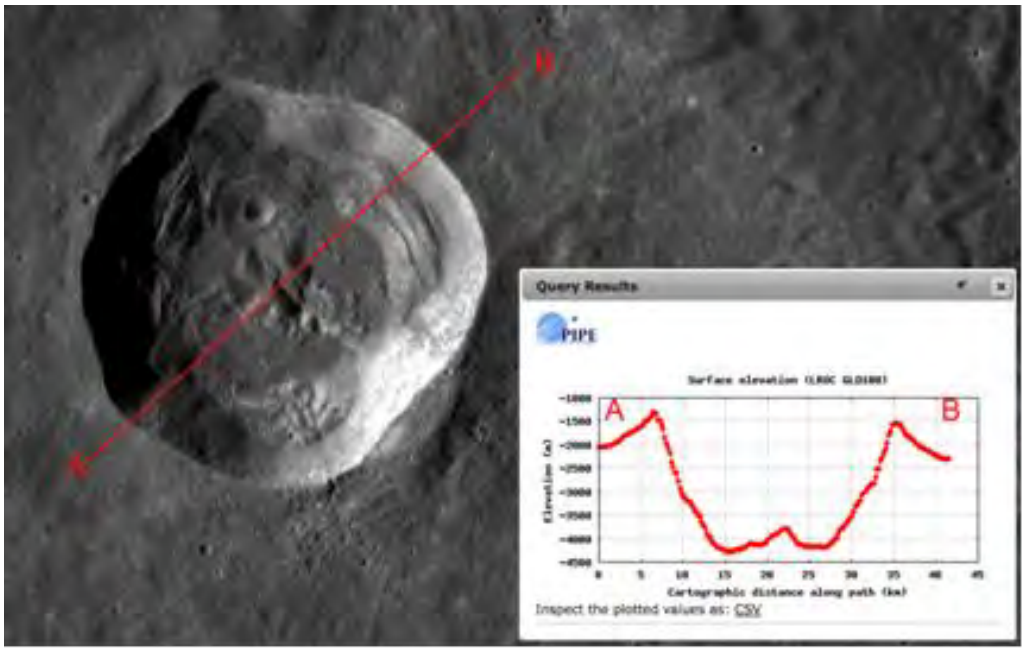

Fig.6 LRO GLD100 profile along line A-B of Madler showing relative heights of up-range and down-range rims.

A further indication of an oblique impact origin in Madler is the relative heights of the proposed up-range (NE) and down-range (SW) rims. As can be seen from Fig.6, the proposed up-range rim to the north-east is depressed by some 200m when compared to the south-western rim, a phenomenon noted in oblique impacts (Herrick and Forsberg-Taylor, 2003).

The different expression of Madler's up-range rays (with the south-eastern one being conspicuous and the northern one all but invisible) may have served to hinder their identification, as more well known examples tend to be more symmetrical as in the case of craters such as Proclus, Tycho and Jackson. In addition to the presence or absence of bright ray material, the two rays proposed here are geometrically asymmetric, with the southern ray being straight, and the northern one being 'arachnid' in profile. There are however a number of examples where an asymmetry is present, indicating that local conditions at the impact site may contribute to the development of up-range rays.

The 22km diameter Harding has a prominent bright curving cardioid ray to the east, but to the north the bright ray is replaced by a dark ray (Fig.7). The symmetry of the dark and light rays is visible when the relative Titanium content is viewed, with both rays demonstrating a relatively lower TiO_2 content than the surrounding terrain, indicating an origin from Low TiO_2 basalts which underly the Higher TiO_2 surface rocks. Some other factor has however rendered the northern ray less conspicuous in terms of albedo than the southern one, making the identification of Harding as an oblique impact crater difficult.

Another example of asymmetry, this time in terms of physical expression is Crookes, an oblique impact crater with the ZoA to the east (Fig.8). This crater exhibits two bright cardioid up-range rays either side of the ZoA, but only the northern ray shows a pronounced chain of overlapping secondary craters proximally. It is worth noting also that this northern crater chain is particularly well developed near the crater rim, consisting of an almost continual trough orientated tangential to the crater rim, and bounded by ridges of ejecta set in a 'herringbone' pattern characteristic of secondary impacts. This feature is highly suggestive of the trough forming

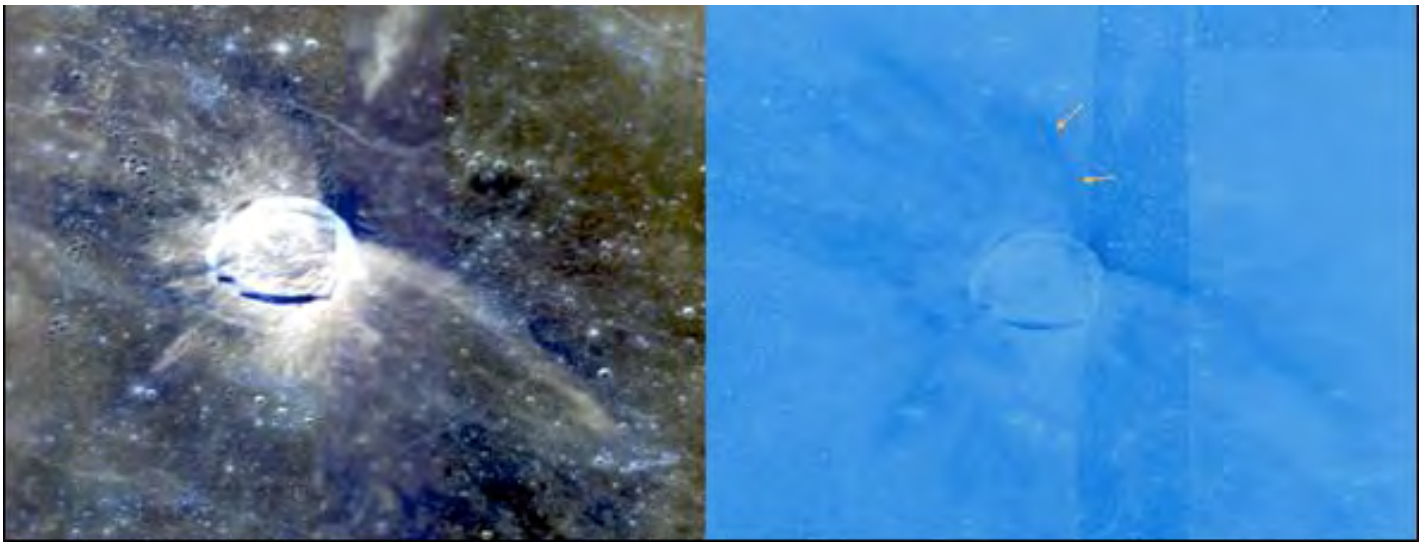

Fig.7 Clementine NIR Multispectral Mosaic of Harding showing the ZoA to the north-east, with brighter southern cardioid ray and darker northern ray (left) and LMMP image of same area showing Low Titanium lithology in dark blue (right).

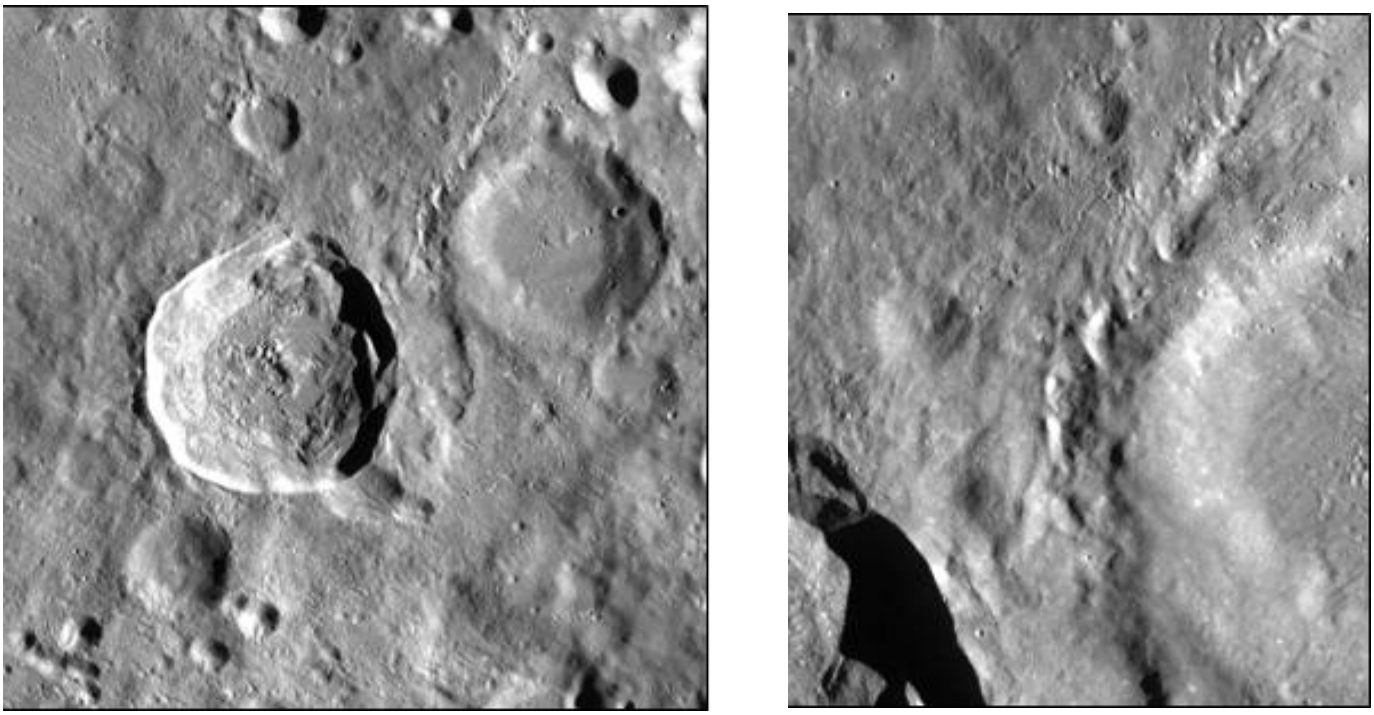

Fig.8 LROC WAC image of Crookes (left) showing cardioid ray to the north and detail of secondary crater chains forming proximal part of the ray (right). Note the absence of a similar crater chain to the south. The ZoA is to the right (east) of the crater.

the proximal part of the northern ray of Madler, suggesting an origin in a similar process.

Both Crookes and Harding illustrate the fact that up-range ray asymmetry can take the form of a difference in albedo or a difference in the development of secondary cratering along the rays. Madler appears to be an example where both effects are be present. The northern ray of Madler appears inconspicuous due to it's low albedo in

comparison to the southern ray. This may be a consequence of local conditions where the geology excavated by the crater differs to the north and south.

A glance at the Clementine UVVIS Ratio Map image of Madler (Fig.9) shows the presence of the northern ray in the form a thin light blue line representing fresh ejecta, similar in composition to the wide fan of ejecta to the north and west. This shows up as a dark mantling in the Clementine UVVIS Multispectral Mosaic images (Fig.1). A similar situation exists in the case of Harding. The northern ray of Madler is also physically different to the southern, consisting of a deep proximal crater chain which changes distally into a subdued and 'feathery' field of secondary craters. The southern ray by contrast exhibits en-echelon secondary craters forming the core of the high albedo bright ray.

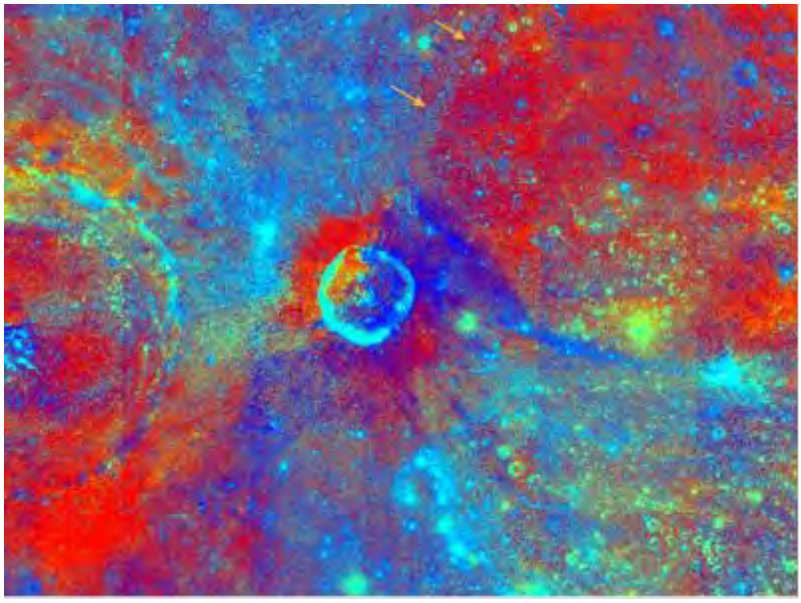

Fig.9 Clementine UVVIS Ratio Map image of Madler showing the northern cardioid ray picked out as a thin blue line (arrows). This appears to be similar to the ejecta seen to the north and west also showing up as light blue. Comparing this image to Fig.1 suggests that the difference in the albedo of the ejecta blanket is a consequence of lithological difference.

Conclusion.

Madler is probably an example of an oblique angled impact crater with the approach direction of the impactor being from the north-east. The distribution of ejecta normally associated with such impacts is not conspicuous here due to the asymmetric development of the up-range rays, and the division of the ejecta into low albedo material to the north and high albedo material to the south. These differences may be a consequence of the local subsurface geology, which being on the rim of the Nectaris Basin may be represented by submerged highland material as well as superimposed mare deposits. The presence of a ZoA to the north-east and a preferential development of both bright and dark ejecta to the south-west supports the conclusions drawn in relation Madlers oblique impact origin. The crater post-dates Theophilus as its dark ejecta can be seen to cover the eastern floor of the larger crater. The distribution of ejecta surrounding oblique impacts can be diagnostic of this type of crater, but asymmetric development, especially in areas of diverse sub surface geology may well obscure these characteristic features.

References:

Herrick, R. R, Forsberg-Taylor N. K. 2003. The shape and appearance of craters formed by oblique impact on the Moon and Venus. Meteoritics & Planetary Science 38, Nr 11, 1551–1578

Milton, D.J, 1968. (LAC-78) Geologic map of the Theophilus quadrangle of the moon. USGS IMAP: 546

Schultz, P.H, Anderson, J.B.L and Hermalyn, B (2009) Origin and significance of uprange ray patterns. 40th Lunar and Planetary Science Conference (2009)

Wood, C. 2009. http://lpod.wikispaces.com/November+28%2C+2009

Acknowledgements:

LROC images, topographic charts and 3D visualisation reproduced by courtesy of the LROC Website, School of Earth and Space Exploration,University of Arizona at: http://lroc.sese.asu.edu/index.html

Clementine Multispectral Images courtesy of the USGS PSD Imaging Node at: http://www.mapaplanet.org/

Selene images courtesy of Japan Aerospace Exploration Agency (JAXA) at: http://l2db.selene.darts.isas.jaxa.jp

Selenology Today

Domes in northern Mare Tranquillitatis: Morphometric analysis and mode of formation

By Raffaello Lena and Paolo Lazzarotti
Geologic Lunar Research (GLR) group

Abstract
In this study we examine lunar mare domes situated to the east of the crater Jansen, in the northern part of Mare Tranquillitatis. Morphometric details were established for three lunar domes, while further seven domes, located between Vitruvius G and Vitruvius M will be the object of a next study. The first dome, named C8, has been previously reported by our group but it is analyzed using GLD100 dataset together to photoclinometry and SfS applied to CCD image of higher detail. Its height was determined to 270 m with an average slope of 2.5°. We determined morphometric data of further two unreported domes, named C18, located at 30.04º E and 14.06º N, and C19 located at 29.92° E and 14.42° N, respectively. C18 has a diameter of 7.2 km, a height of 125 m and an average slope of 1.9°. For C19 we determined a diameter of 4 km, a height of 70 m, a flank slope of 2.0°. According to the GLR classification scheme both domes C8 and C18 belong to class C_2, while C19 belong to class E_1 with a tendency towards class A. Based on rheologic modelling of the domes and a viscoelastic model of the feeder dikes, we obtained magma viscosity, effusion rate and duration of the effusion process for C8 (4.3×10^6 Pa s, 101 $m^3 s^{-1}$, 5.3 years), C18 (3.6×10^5 Pa s, 74 $m^3 s^{-1}$, 1.2 years) and C19 (9.0×10^4 Pa s, 40 $m^3 s^{-1}$, 0.34 years). Accordingly we have estimated the magma rise speed (7.3×10^{-6}, 2.2×10^{-5} and 3.9×10^{-5} m s^{-1}), the width of the feeder dike (80, 30 and 15 m) and the dike length (180, 125 and 70 km) for C8, C18 and C19, respectively.

1. Introduction

The apparent internal origin of lunar domes was a major factor in endogenic interpretations of the maria, and their low profiles suggest a volcanism characteristic of fluid mafic magmas [1]. In previous works we have introduced a novel classification scheme for effusive lunar domes which is based on their spectral and morphometric properties, and have examined for a variety of lunar mare domes the relationship between the conditions in the magma source regions and the resulting eruption conditions at the surface [2-3]. The Geologic Lunar Research (GLR) group has an ongoing project to study lunar domes with the purpose of their classification based on rheologic properties [4]. Our Lunar Dome Catalogue is continuously updated according to ongoing observing and modelling activities. In this paper, we describe the results of a survey made on the Cauchy-Vitruvius region in order to characterize further lunar domes examining their morphometric properties. The current study describes three domes, located to the east of the crater Jansen and south of the crater Jansen L, in the northern part of Mare Tranquillitatis, while further seven domes identified near the craters Vitruvius G and M (under ongoing analysis) will be the object of a next report.

2. Ground-based observations

A telescopic CCD image of the examined lunar region is shown in Fig. 1. The image was taken under oblique illumination conditions by Lazzarotti using a Gladius XLI Cassegrain with aperture of 400 mm f/16 and a Baader Zeiss 2x Barlow lens. For image acquisition an experimental Sony ICX285 based CCD camera was employed. The image was taken on September 17, 2011 at 03:48 UT.

The scale of the images is 250 m per pixel on the lunar surface. Due to atmospherical seeing, however, the effective resolution (corresponding to the width of the point spread function) is not much better than 0.7 km.

Some domes have already been measured in previous our studies (e.g. the domes termed C8 and C17 in Fig. 2), and described by GLR group in [4]. However, the dome C8 shown in Fig. 1, has higher resolution than our old image, while further two domes, termed C18 and C19, have not being characterized in our previous studies (cf. Fig. 2).

Figure 1.
Telescopic CCD image made on September 17, 2011 at 03:48 UT (Gladius XLI Cassegrain with aperture of 400 mm f/16 and a Baader Zeiss 2x Barlow lens).

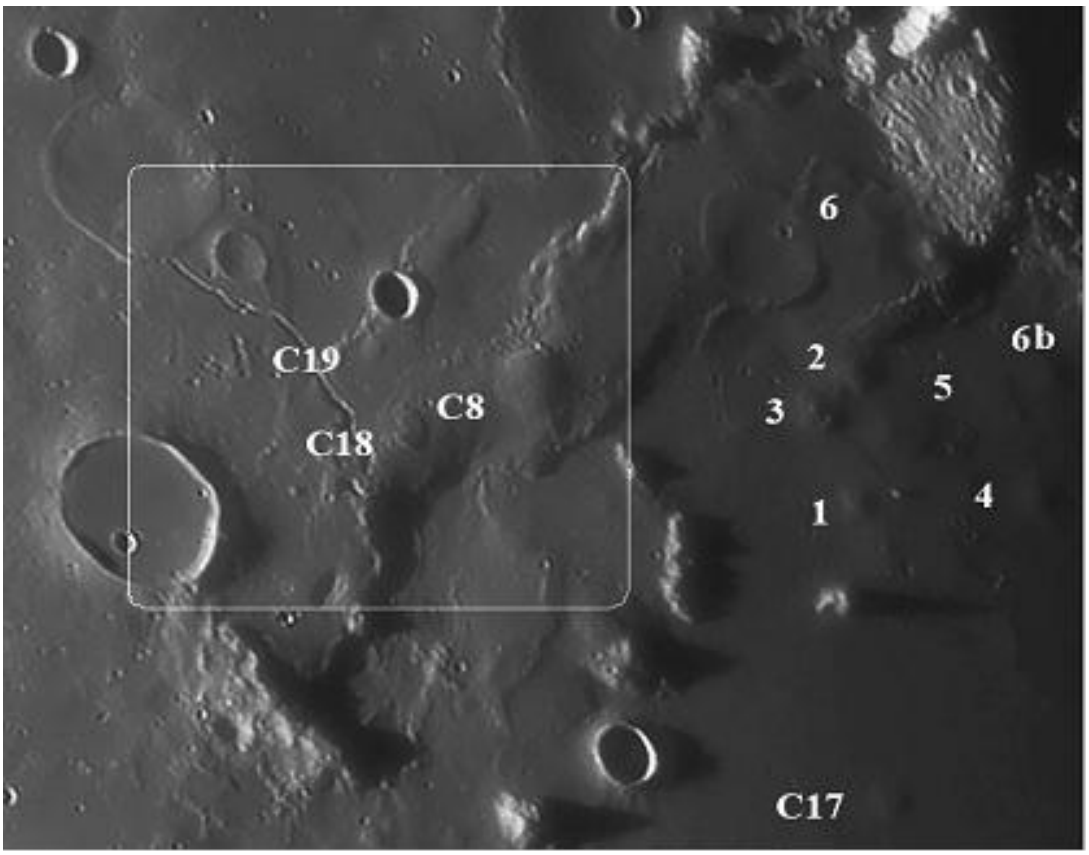

Figure 2.
Examined lunar region marked with a square including the position of the domes termed C8, C18 and C19.

Using the Lunar Terminator Visualization Tool (LTVT) software package [5], we determined the selenographic positions of the examined domes. LTVT is a freeware program that displays a wide range of lunar imagery and permits a variety of highly accurate measurements in these images. Selenographic coordinates, sizes, solar altitudes and shadow lengths of features can be estimated based on a calibration procedure. This calibration, based on ULCN 1994 data, allows LTVT to make the spatial adjustments necessary to bring the observed positions of lunar features into conformity with those expected from the Unified Lunar Control Network (ULCN). The ULCN is a set of points on the lunar surface whose three-dimensional selenodetic coordinates (latitude, longitude, and radial distance from the lunar centre) have been determined by careful measurement. Typically these points consist of very small craters. According to [6], the three-dimensional positions are expressed in the mean Earth/polar axis system.

3. WAC (LRO) imagery

The Lunar Reconnaissance Orbiter (LRO) WAC image (cf. Fig 3) displays the examined domes, some of them characterized by the presence of some non-volcanic hills or ridges on the summit.

4. Methods, measurements and material

1. For spectral analysis we utilise the Clementine UVVIS five-band data set as published in [7]. For all spectral data extracted in this study, the size of the sample area on the lunar surface was set to 2 × 2 km^2. Variations in soil composition, maturity, particle size, and viewing geometry are indicated by the reflectance R_{750} at 750 nm wavelength. Another important spectral parameter is the R_{415}/R_{750} ratio, which is correlated with the variations in TiO_2 content of mare soils. A corresponding relation was established by Charette et al., specifically regarding different basaltic units in Mare Tranquillitatis [8].

A comprehensive characterisation of spectral features attributable to titanium in lunar soils is provided in [9]. The third regarded spectral parameter, the R_{950}/R_{750} ratio, is related to the strength of the mafic absorption band, representing a measure for the FeO content of the soil and being also sensitive to the optical maturity of mare and highland materials [10]. The spectral data of the examined domes are listed in Table 1.

The corresponding Clementine color ratio map is shown in Fig. 4. In the Clementine color ratio the

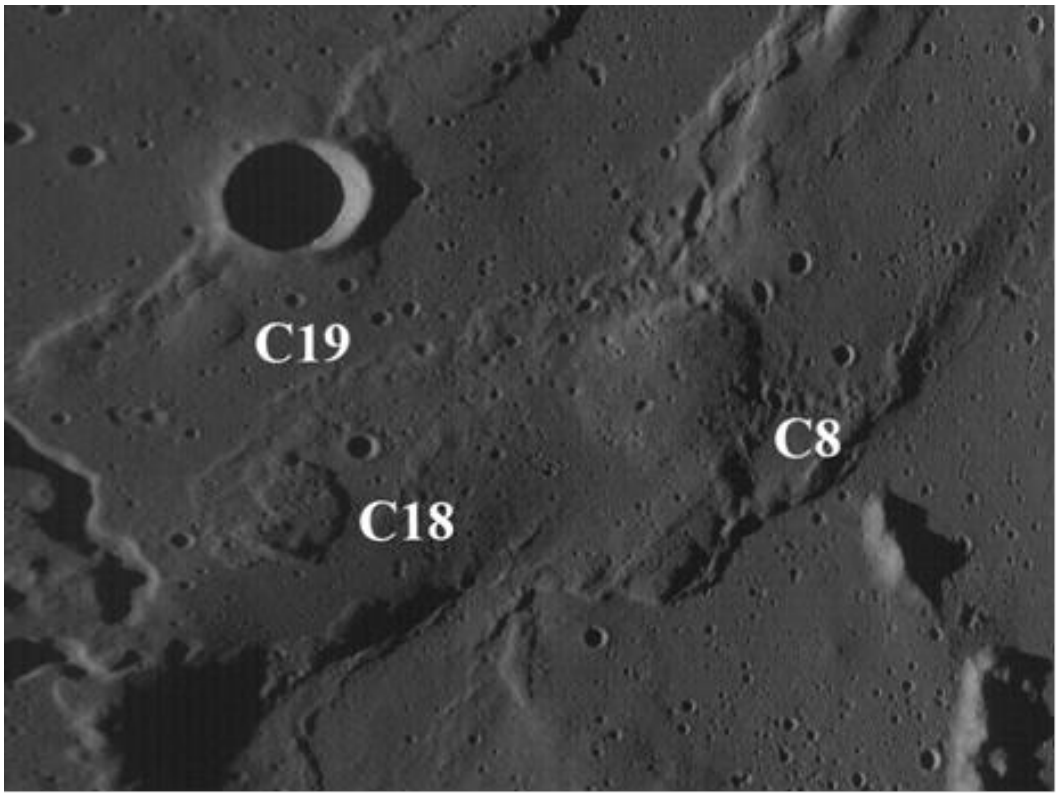

Figure 3.
WAC imagery of the examined lunar mare domes.

maria are depicted in yellow/orange (iron-rich, lower titanium) or blue (iron-rich, higher titanium). C8 is characterized by a different color respect to the nearby soil and appears reddish indicating an decreased TiO_2 content if compared with the domes C18 and C19, which are spectrally bluer with higher R_{415}/R_{750} ratios. For the elemental abundance wt% of the lunar region described in this study, we have applied the TiO_2 and FeO estimation equations, by Lucey et al., described in [11].

2. We have generated a digital elevation model (DEM) of the examined domes based on our telescopic CCD image. A well-known image-based method for 3D surface reconstruction is shape from shading (SfS). The SfS approach aims for deriving the orientation of the surface at each image location by using a model of the reflectance properties of the surface and knowledge about the illumination conditions, finally leading to an elevation value for each image pixel [12]. The height values were obtained by determining elevation differences between the summit of the dome and its surrounding on the corresponding 3D profiles derived by photoclinometry and shape from shading analysis, as described in our previous works [4].

3. Scholten et al. present a nearly global lunar DEM with a grid size of 100 m, the so-called GLD100 [13]. This DEM has been constructed based on photogrammetric analysis of LROC WAC image pairs. According to [13], the average elevation accuracy of the GLD100 amounts to 20 m, while 10 m accuracy is achieved for the nearside mare regions. ACT-REACT Quick Map tool was used to access to the GLD100 dataset, allowing to obtain the cross-sectional profiles and the corresponding 3D views. The 3D reconstructions are obtained using WAC mosaic draped on top of the global WAC-derived elevation model (GLD100). The morphometric properties are listed in Table 2.

4. Wilson and Head provide a quantitative treatment of such dome-forming eruptions [14]. This model estimates the yield strength τ , i. e. the pressure or stress that must be exceeded for the lava to flow, the plastic viscosity η, yielding a measure for the fluidity of the erupted lava, the effusion rate E, i. e. the lava volume erupted per second, and the duration T = V/E of the effusion process. This model is applied to a large set of representative lunar mare domes in [2, 4]. It relies on the morphometric dome properties (diameter, height, volume) and several physical constants such as the lava density, the acceleration due to gravity, and the thermal diffusivity of the lava. The computed values for $\boldsymbol{\tau, \eta,}$ E, and T obtained with the rheologic model [14] are valid for domes that formed from a single flow unit (monogenetic volcanoes). Otherwise, the computed rheologic values are upper limits to the respective true values. Furthermore, we estimated the magma rise speed U and the dike geometry (width W and length L) according to the model developed in [15]. These models have been routinely used for estimating the rheologic properties and dike geometries for a large number of monogenetic lunar mare domes by our previous studies [2, 3, 4, 16], where more detailed explanations can be found.

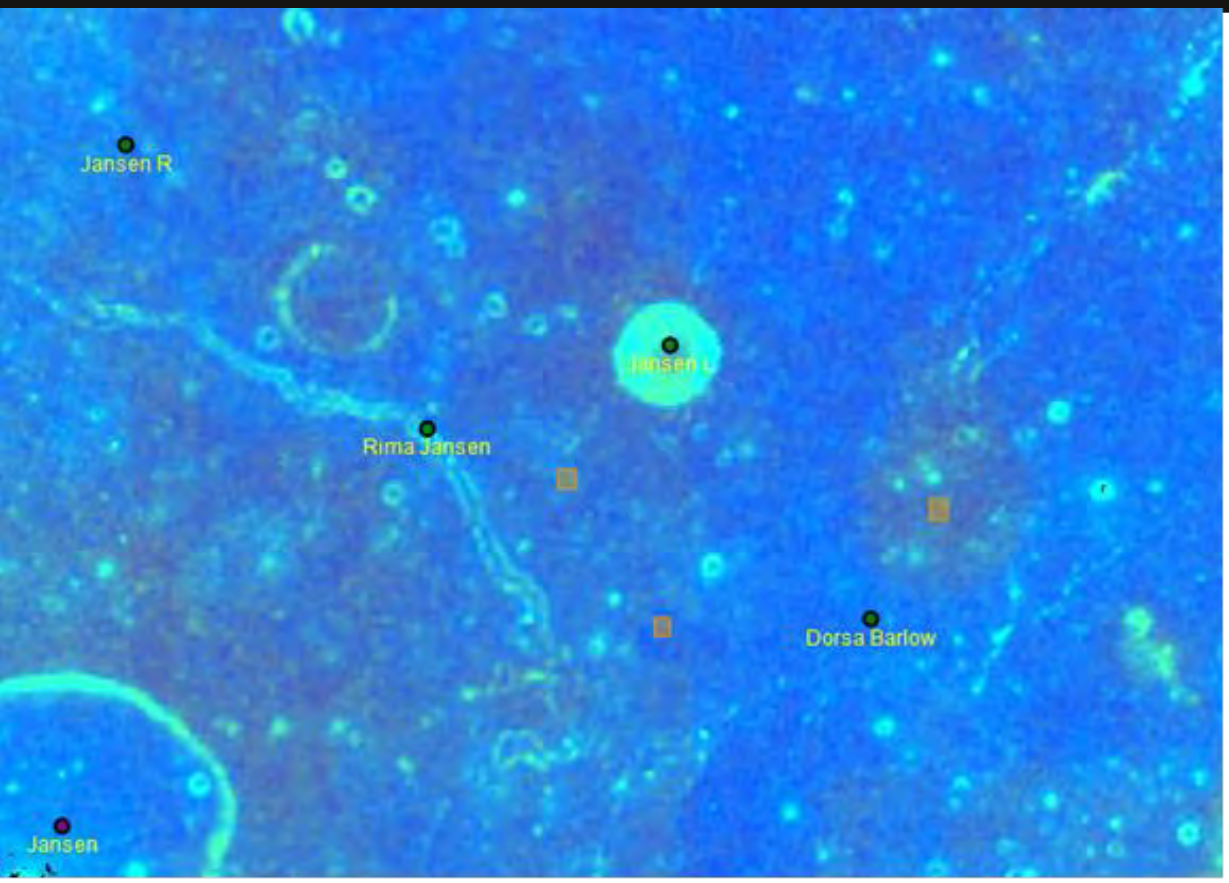

Figure 4.
Clementine color ratio image, including the location of the domes where the spectral data were acquired.
Clementine false color map obtained assigning the R_{750}/R_{415}, R_{750}/R_{950} and R_{415}/R_{750} into the red, green, and blue channels, respectively.

5. Results and discussion

5.1 Morphometric properties and spectral analysis

Dome C8

The dome termed C8 has been previously reported by GLR group [4]. However, the image shown in Fig. 1 displays the dome in higher detail of our previous data. Thus, We have re-analyzed C8 by using GLD100 dataset [13]. The dome is located at 30.76º E and 14.32º N, with a diameter of 12.5 km ± 0.3 km.
The effective height of the dome, computed by using the photoclinometry and shape from shading method applied to CCD terrestrial image, was obtained by determining elevation differences between the summit of the dome and its surroundings, taking into account the curvature of the lunar surface. This leads to a dome height of 270 ± 30 m, yielding an average flank slope of 2.5° ± 0.2° (Fig. 5). The dome edifice volume is determined to 17 km³.
Fig. 6 shows the corresponding cross sectional profile in E-W direction obtained by GLD100 dataset. Accordingly, C8 is 270 m high and its average slope angle corresponds to 2.5°. Hence, based on new analyzed data, we confirm the previous morphometric properties of C8 reported in [4]. The corresponding 3D reconstruction derived by ACT react quick map is shown in Fig. 7. The rheologic model yields an effusion rate of 101 $m^3\ s^{-1}$ and lava viscosity of 4.3 x 10^6 Pa s. It formed over a period of time of 5.2 years.
The Clementine UVVIS spectral data of the dome reveal a 750 nm reflectance of R_{750} = 0.0984, a moderate value for the UV/VIS colour ratio of R_{415}/R_{750} = 0.6337, indicating a moderate to high TiO_2 content, and a weak mafic absorption with R_{950}/R_{750} = 1.0562, indicating a high soil maturity.
According to the classification scheme for lunar domes [2, 4] this dome belongs to class C_2.

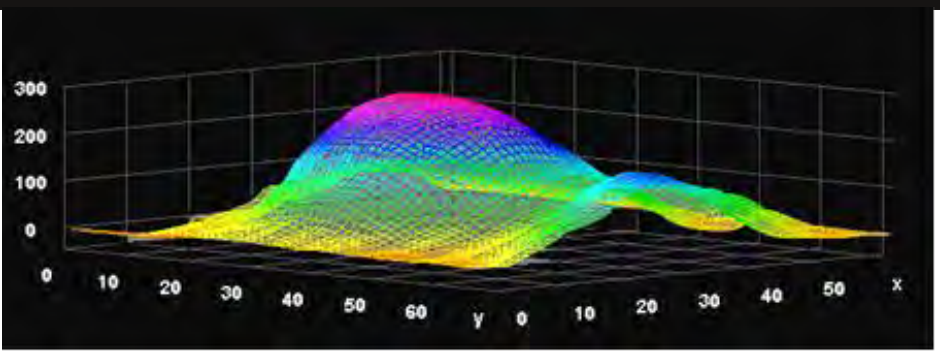

Figure 5.
3D reconstruction of the dome C8, based on terrestrial CCD image by photoclinometry and SfS analysis. The vertical axis is 10 times exaggerated.

Figure 6.
LRO WAC-derived surface elevation plot of a east to west cross-section of the dome C8.

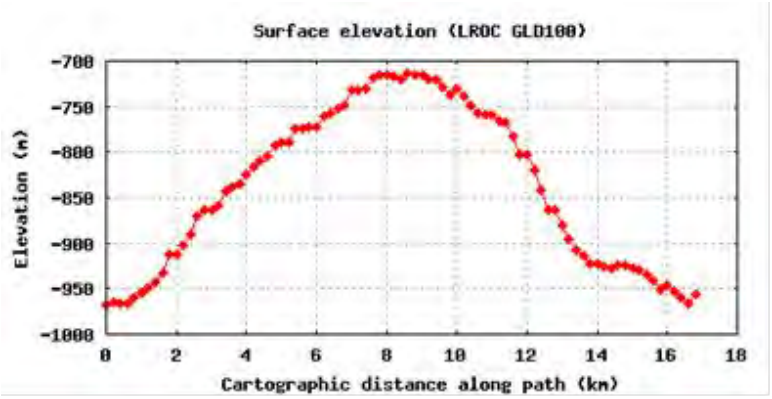

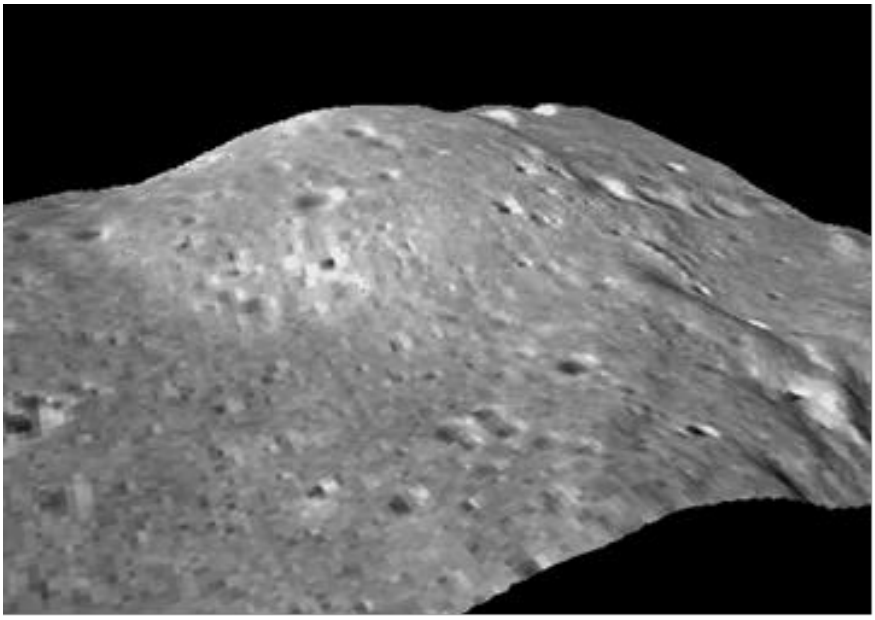

Figure 7.
WAC monochrome mosaic draped on top of the global LROC WAC-derived elevation model (GLD100). 3D reconstruction of the dome C8.

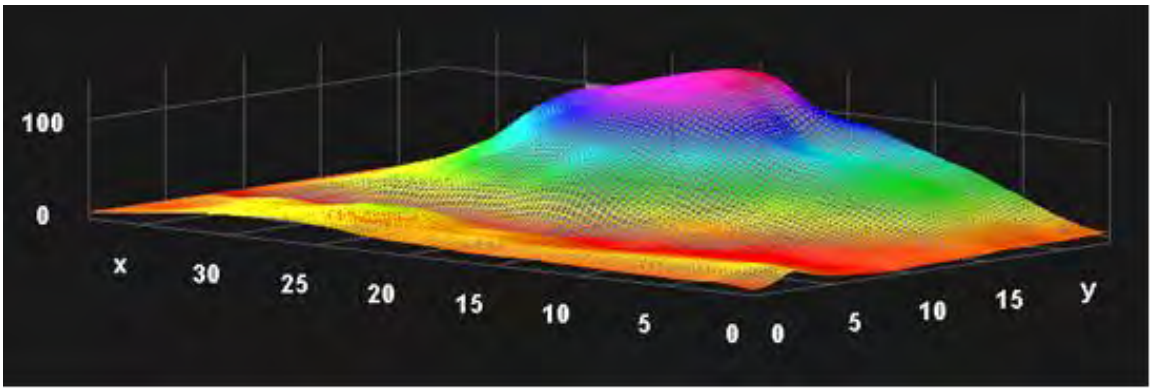

Figure 8.
3D reconstruction of the dome C18, based on terrestrial CCD image by photoclinometry and SfS analysis. The vertical axis is 10 times exaggerated.

Dome C18

In the current study, we describe the dome termed C18, located to the west of C8, at coordinates 30.04 º E and 14.06º N, with a base diameter of 7.2 km ± 0.3 km. Some prominences, presumably non-volcanic hills and ridges, are situated on the summit.

The height was determined to 125 m ± 15 m yielding an average flank slope of 1.9° ± 0.2° (Fig. 8). The edifice volume is determined to 2.9 km³.

The height of the dome was also computed from Fig. 1 using the shadow length method according to the relation h = l tan α, where l is the shadow length, corrected for foreshortening and measured in km, and tan α the tangent of the solar altitude. A height of 110 ± 10 m was obtained. This value is slightly lower than the height values obtained with the photoclinometry and shape from shading method since the shadow only partially covers the flank of the dome and therefore does not account for the full dome height.

Fig. 9 shows the corresponding cross sectional profile in E-W direction obtained by GLD100 dataset. According to results obtained by photoclinometry and shape from shading, it is 125 m high and its average slope angle corresponds to 1.9°. The 3D reconstruction derived by ACT react quick map is shown in Fig. 10.

The rheologic model applied to C18 dome yields an effusion rate of 74 m^3 s^{-1} and lava viscosity of 3.6 x 10^5 Pa s. It formed over a period of time of 1.2 years.

The Clementine UVVIS spectral data of the dome reveal a lower 750 nm reflectance of R_{750} = 0.0858, a moderate value for the UV/VIS colour ratio of R_{415}/R_{750} = 0.6320, indicating a moderate to high TiO_2 content, and a weak mafic absorption with R_{950}/R_{750} = 1.0503, indicating a high soil maturity.

According to the classification scheme for lunar domes also this dome belongs to class C_2.

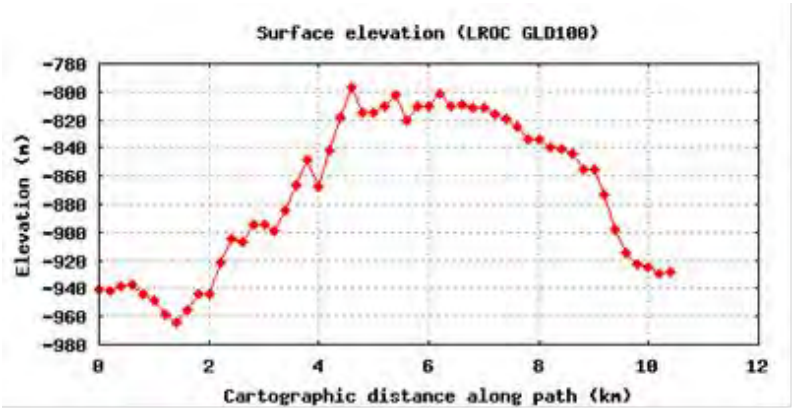

Figure 9.
LRO WAC-derived surface elevation plot of a east to west cross-section of the dome C18.

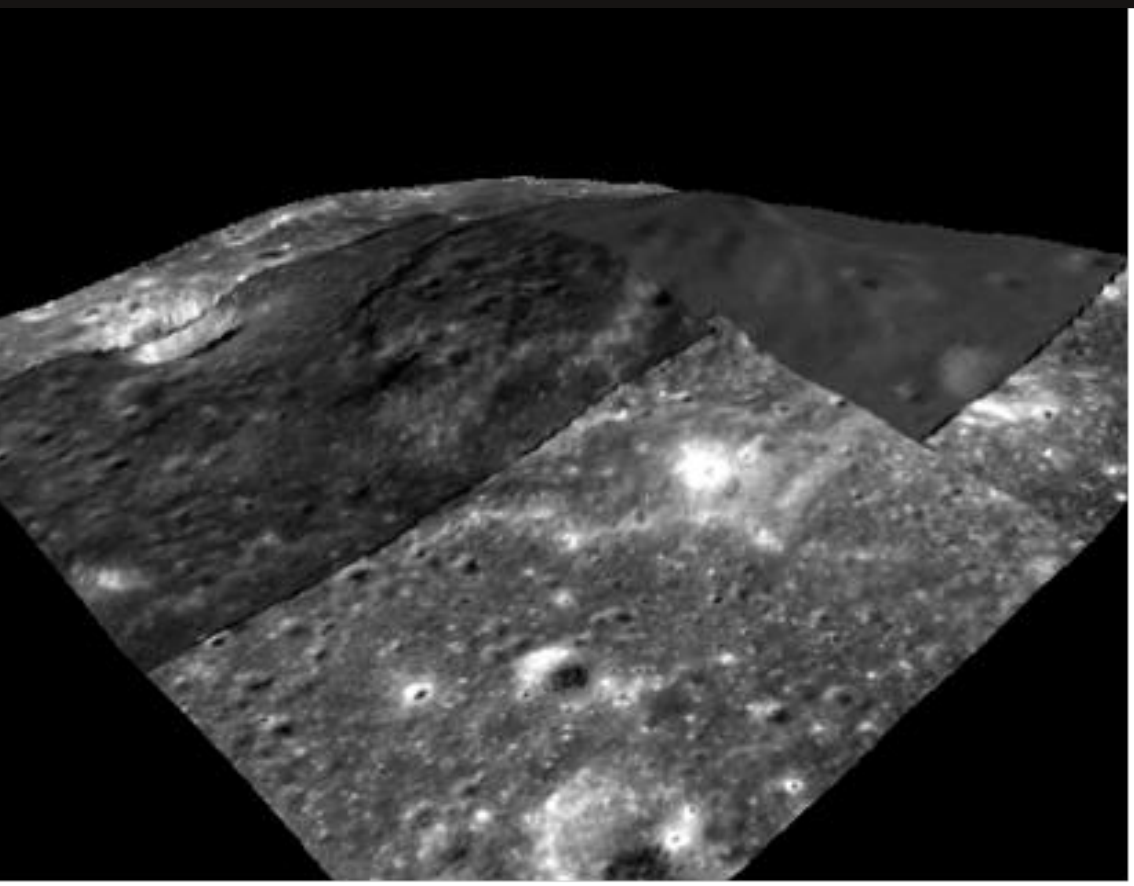

Figure 10.
WAC monochrome mosaic draped on top of the global LROC WAC - derived elevation model (GLD100). 3D reconstruction of the dome C8.

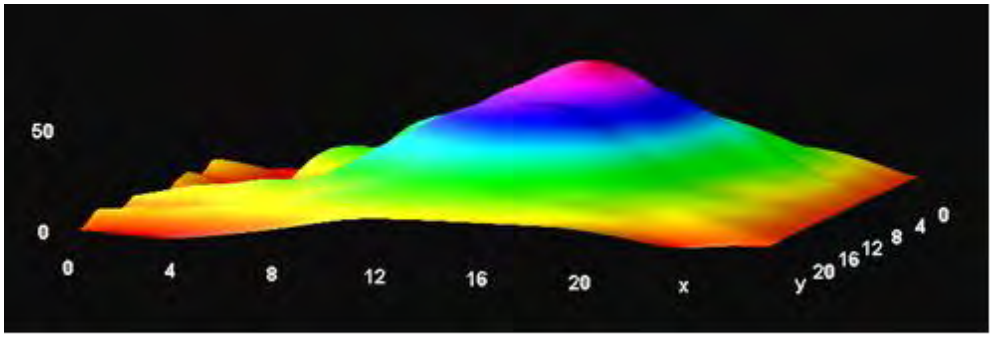

Figure 11.
3D reconstruction of the dome C19, based on terrestrial CCD image by photoclinometry and SfS analysis. The vertical axis is 10 times exaggerated in the meshed reconstruction.

Dome C19

This low dome is located at 29.92° E and 14.42° N. Based on the images shown in Figs. 11-13, the height of C19 dome was determined to 70 ± 10 m, resulting in an average slope of 2.0° ± 0.2°. The diameter amounts to 4.0 ± 0.3 km and the volume to 0.6 km^3. The rheologic model yields an effusion rate of 40 $m^3 s^{-1}$. It was formed from lava of viscosity of 9.0 x 10^4 Pa s, over a period of time of 0.34 years (about 4 months). The Clementine UVVIS spectral data of the dome reveal a lower 750 nm reflectance of R_{750} = 0.0942, R_{415}/R_{750} = 0.6418, indicating a higher TiO_2 content, and a weak mafic absorption with R_{950}/R_{750} = 1.0487.
According to the classification scheme for lunar domes [2-4] C19 falls between classes A and E_1, principally due to its flank slope (2°) and higher R_{415}/R_{750} colour ratio.

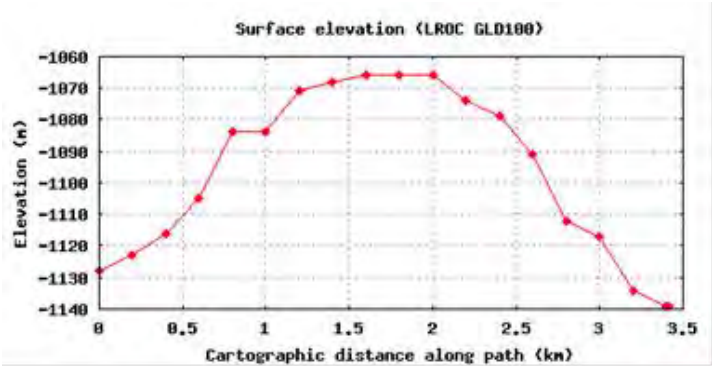

Figure 12.
LRO WAC-derived surface elevation plot of a east to west cross-section of the dome C19.

5.2 TiO2 and FeO contents of the examined domes and petrographic map

We have applied the TiO_2 and FeO estimation equations reported in [11]. The derived values for FeO and TiO2 are then converted to Fe and Ti elemental abundance by multiplication for the factor (56/72) and (48/80) respectively, according to the atomic weights of the constituent elements. According to the Clementine color ratio images, the Ti map indicates that the dome C8 has a TiO_2 contents between 8.0 and 10.0 wt% corresponding to a Ti content of 4.8-6.0 wt%. The elemental abundances of C18 and C19 correspond to a higher TiO_2 content. For the dome C18 we have computed a value of 10.5-11.3 wt% (6.3-6.8 wt % as Ti), while the dome C19 has a TiO_2 contents of 9.9-11.4 wt% (5.9-6.9 wt % as Ti). The corresponding map for the TiO_2 Wt% abundance is reported in Fig. 14. The Fe map, obtained with the method described in [11], shows that C8 has a FeO contents between 16.8 wt% and 18.0 wt% (13.1 wt%-14.0 wt% as Fe), with a slightly higher FeO contents (18.2-18.8 wt%) for the domes C18 and C19. Fig. 15 displays the corresponding map for the FeO wt% .

Figure 13.
WAC monochrome mosaic draped on top of the global LROC WAC-derived elevation model (GLD100). 3D reconstruction of the dome C19.

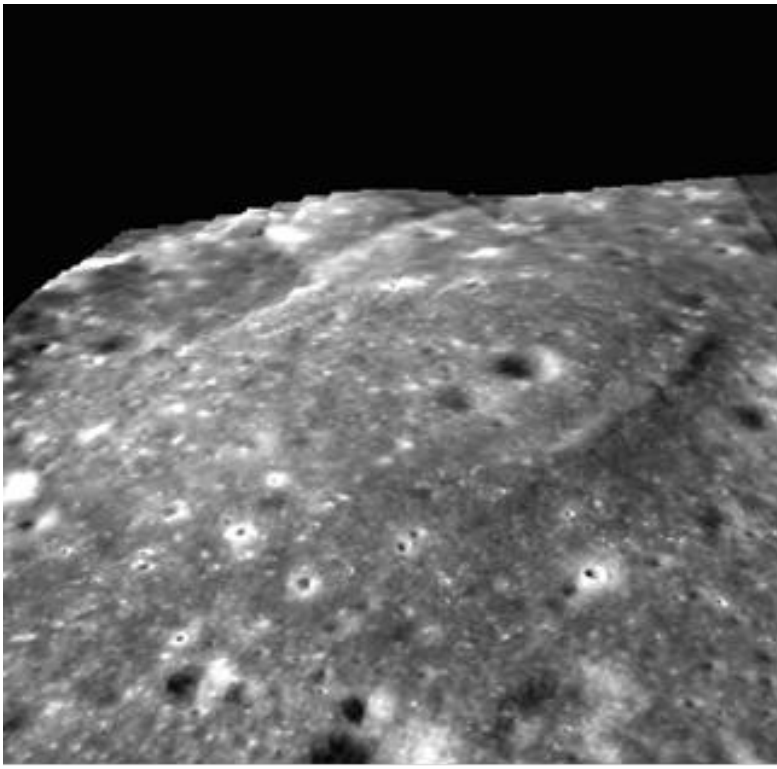

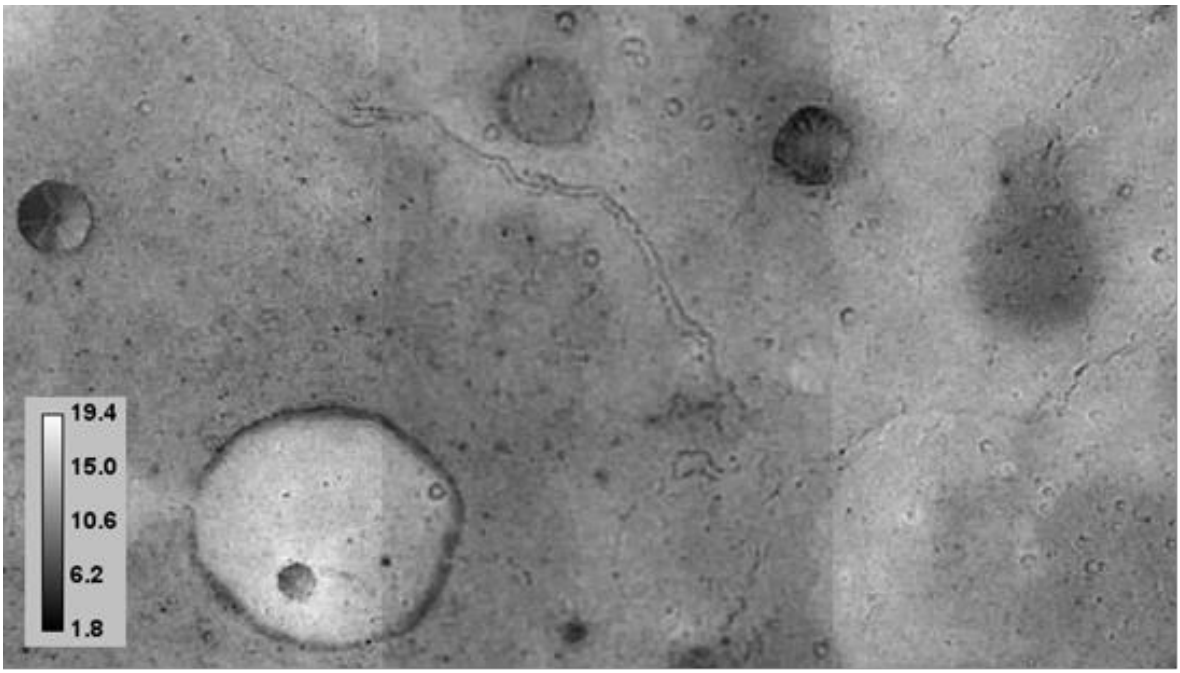

Figure 14.
TiO_2 map of the examined region, including the domes, obtained with the method described by Lucey et al. (2000) in [11].

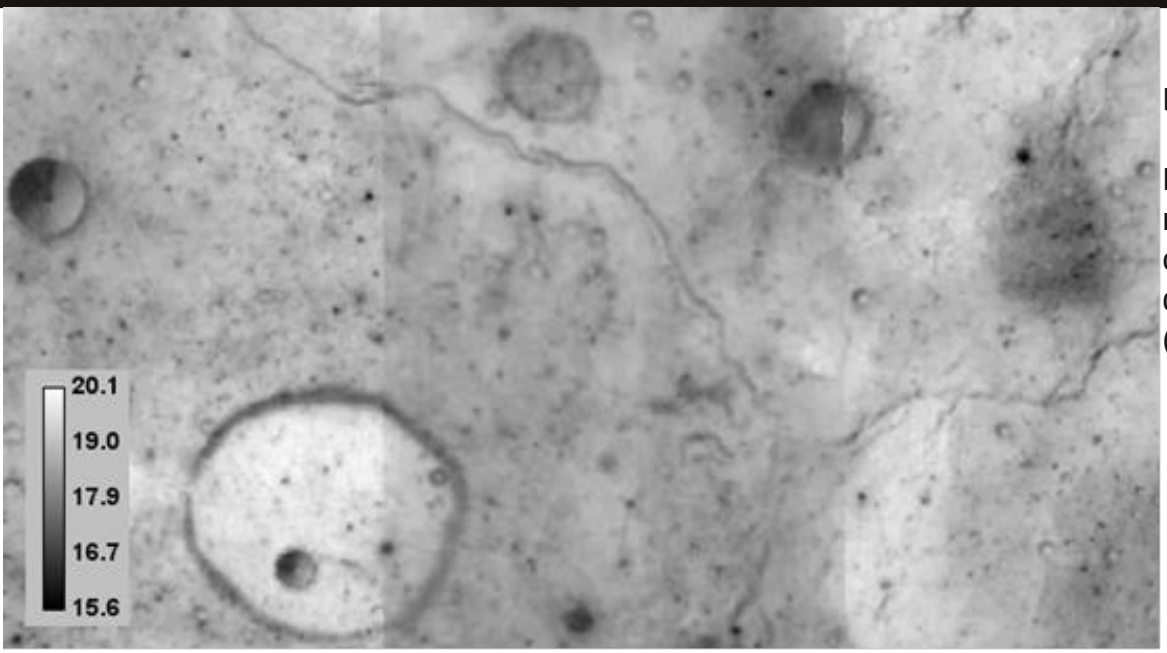

Figure 15.

FeO map of the examined region, including the domes, obtained with the method described by Lucey et al. (2000) in [11].

We have generated a petrographic map (Fig. 16) of the region under study, based on the method described in [17]. The petrographic map indicates the relative fractions of the three endmembers mare basalt (red channel), Mg-rich rock (green channel), and ferroan anorthosite (FAN, blue channel).

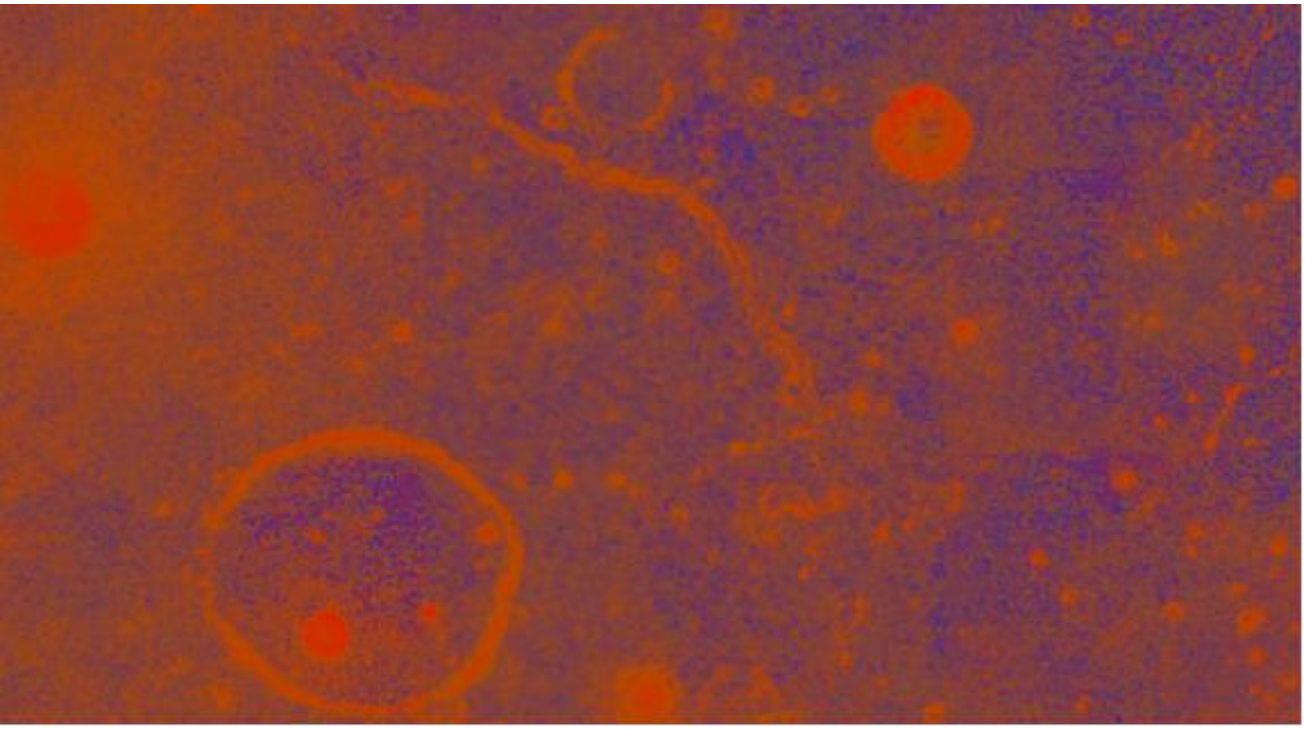

Figure 16.

Petrographic map of the examined region.

5.3 Eruption conditions and mode of emplacement

Based on the spectral and morphometric data obtained in this study, the domes C8 and C18 belong to class C_2.

According to the GLR classification scheme, class C domes have diameters between 8 and 20 km. Domes formed from spectrally red lavas of low to moderate R_{415}/R_{750} ratio with large diameters between 13 and 20 km and large edifice volumes of several tens of km^3 are assigned to subclass C_1, while spectrally bluer domes of moderate to high R_{415}/R_{750} ratio, smaller diameters between 8 and 13 km, and lower edifice volumes are assigned to subclass C_2.

Both domes consist of lavas of intermediate to high viscosity, erupting at intermediate effusion rates. If the effusion process continues over a long period of time, steep flank slope and higher edifice volume may occur as in the case of C8, while short durations of the effusion process result in lower edifices of lower volume, as it is the case for the dome C18.

The third examined dome C19, characterized by lower height and smaller diameter of 4 km, was formed during shorter effusion time and falls between class A and E_1.

The class E domes represent the smallest volcanic edifices formed by effusive mechanisms observed to date (subdivided into subclasses E_1 and E_2 denoting the steep-sided flank slope and the shallow edifices of this class, respectively), while the class A is composed by domes with low flank slopes (< 1°) but consisting of spectrally blue (high R_{415}/R_{750} ratio > 0.64) lava.

Regarding the mode of emplacement of effusive lunar mare domes three rheologic groups have been introduced in [4]. The first group, R_1, is characterised by lava viscosities of 10^4-10^6 Pa s, magma rise speeds of 10^{-5} – 10^{-3} m s^{-1}, dike widths around 10-30 m, and dike lengths between about 30 and 200 km. Rheologic group R_2 is characterised by low lava viscosities between 10^2 and 10^4 Pa s, fast magma ascent (U > 10^{-3} m s^{-1}), narrow (W = 1-4 m) and short (L = 7-20 km) feeder dikes.

The third group, R_3, is made up of domes which formed from highly viscous lavas of 10^6-10^8 Pa s, ascending at very low speeds of 10^{-6}-10^{-5} m s^{-1} through broad dikes of several tens to 200 m width and 100-200 km length.

The dome C8 is a typical representative of rheologic group R_3. It is characterised by lava viscosity of about 4.3 x 10^6 Pa s, with computed magma rise speed of 7.3 x 10^{-6} m s^{-1}, dike width of 80 m and dike length of 180 km. On the contrary the domes C18 and C19, characterized by lower lava viscosity are representative of rheologic group R_1, with computed magma rise speed of 2.2 x 10^{-5} and 3.9 x 10^{-5} m s^{-1}, respectively, erupting through dikes 30 and 15 m wide, 125 and 70 km long. Hence, for the examined domes the magma reservoirs are located well below the lunar crust regarding the thicknesses of the total and upper crust of 55 and 32 km, respectively, in northern Mare Tranquillitatis [18].

6. Summary and conclusion

In this study we have performed an analysis of the morphometric and spectral properties of three lunar domes. C8 is 270 m high and its average slope amounts to 2.5° and its diameter is determined of 12.5 km. C18 has a diameter of 7.2 km, a height of 125 m and an average slope of 1.9°. For C19 we determined a diameter of 4 km, a height of 70 m, a flank slope of 2.0°. According to the morphometric data and spectral analysis C8 and C18 belong to class C_2, while C19 belong to class E_1 with a tendency towards class A. The dome C8, characterised by lava viscosity of 4.3 x 10^6 Pa s, is a typical representative of rheologic group R_3 as introduced in [3-4], while C18 and C19, originated by lower lava viscosity and are representative of rheologic group R_1. Furthermore we have inferred the titanium content of the examined domes, characterized by moderate to high TiO_2. Based on a

viscoelastic model of the feeder dikes we determined the corresponding magma rise speed, width of the feeder dike and the dike length for C8, C18 and C19, respectively. These estimates indicate that the magma reservoirs are located well below the lunar crust regarding the thicknesses of the total and upper crust in northern Mare Tranquillitatis.

Dome	R_{415}	R_{750}	R_{415}/R_{750}	R_{950}/R_{750}
C8	0.0624	0.0984	0.6337	1.0562
C18	0.0543	0.0858	0.6320	1.0503
C19	0.0605	0.0942	0.6418	1.0487

Table 1

Spectral properties of the domes C8, C18 and C19, derived from Clementine UVVIS data.

Dome	h [m]	slope [°]	size [km]	V [km³]	E [$m^3 s^{-1}$]	η [Pa s]	T [years]
C8	270	2.5	12.5	17	101	4.3×10^6	5.3
C18	125	1.9	7.2	2.9	74	3.6×10^5	1.2
C19	70	2.0	4.0	0.6	40	9.0×10^4	0.34

Table 2

Morphometric properties of the domes C8, C18 and C19 and results for Effusion rate (E), lava viscosity (η) and the effusion time (T).

Selenology Today

References

[1] Wilhelms, D. E., 1987. The geologic history of the Moon. USGS Professional Paper 1348.
[2] Wöhler, C., Lena, R., Lazzarotti, P., Phillips, J., Wirths, M., & Pujic, Z., 2006. A combined spectrophotometric and morphometric study of the lunar mare dome fields near Cauchy, Arago, Hortensius, and Milichius. Icarus, 183, 237–264.
[3] Wöhler, C., Lena, R., & Phillips, J., 2007. Formation of lunar mare domes along crustal fractures: Rheologic conditions, dimensions of feeder dikes, and the role of magma evolution. Icarus, 189 (2), 279–307.
[4] Lena, R., Wöhler, C., Phillips, J., Chiocchetta, M.T., 2013. Lunar domes: Properties and Formation Processes, Springer Praxis Books.
[5] Mosher, J., & Bondo, H., 2006. Lunar Terminator Visualization Tool (LTVT). http://inet.uni2.dk/ d120588/henrik/jim ltvt.html
[6] Davies, M. E., Colvin, T. R., Meyer, D. L., & Nelson, S., 1994. The unified lunar control network: 1994 version. Journal of Geophysical Research, 99 (E11), 23211–23214.
[7] Eliason, E., Isbell, C., Lee, E., Becker, T., Gaddis, L., McEwen, A., & Robinson, M., 1999. Mission to the Moon: the Clementine UVVIS global mosaic. PDS Volumes USA NASA PDS CL 4001 4078. http://pdsmaps.wr.usgs.gov
[8] Charette, M. P., McCord, T. B., Pieters, C., & Adams, J. B., 1974. Application of remote spectral reflectance measurements to lunar geology classification and determination of titanium content of lunar soils. Journal of Geophysical Research, 79 (11), 1605–1613.
[9] Burns, R. G., Parkin, K. M., Loeffler, B. M., Leung, I. S., & Abu-Eid, R. M., 1976. Further characterization of spectral features attributable to titanium on the moon. Lunar Science Conference 7, pp. 2561–2578.
[10] Lucey, P. G., Blewett, D. T., & Hawke, B. R., 1998. Mapping the FeO and TiO2 content of the lunar surface with multispectral imagery. Journal of Geophysical Research, 103 (E2), 3679–3699.
[11] Lucey, P.G., Blewett, D.T., Jolliff, B.L., 2000. Lunar iron and titanium abundance algorithms based on final processing of Clementine ultraviolet-visible images. J. Geophys. Res. 105 (E8), 20297–20306.
[12] Horn, B. K. P., 1989. Height and Gradient from Shading. MIT technical report 1105A. http://people.csail.mit.edu/people/bkph/AIM/AIM-1105A-TEX.pdf
[13] Scholten, F., Oberst, J., Matz, K.-D., Roatsch, T., Wählisch, M., Speyerer, E.J., Robinson, M.S., 2012. GLD100: the near-global lunar 100 m raster DTM from LROC WAC stereo image data. J. Geophys. Res. 117(E00H17). doi: 10.1029/2011JE003926.
[14] Wilson, L., Head, J.W., 2003. Lunar Gruithuisen and Mairan domes: rheology and mode of emplacement. J. Geophys. Res. 108(E2), 5012–5018.
[15] Rubin, A. S., 1993. Tensile fracture of rock at high confining pressure: Implications for dike propagation. J. Geophys. Res. 98, 15919-15935.
[16] Lena, R., Wöhler, C., Phillips, J., Wirths, M., Bregante, M. T., 2007. Lunar domes in the Doppelmayer region: Spectrophotometry, morphometry, rheology, and eruption conditions. Planetary and Space Science 55, pp. 1201-1217.
[17] Wöhler, C., Berezhnoy, A., Evans, R., 2011. Estimation of Elemental Abundances of the Lunar Regolith Using Clementine UVVIS+NIR Data. Planetary and Space Science, vol. 59, no. 1, pp. 92-110. DOI 10.1016/j.pss.2010.10.017
[18] Wieczorek, M. A., B. L. Jolliff, A. Khan, M. E. Pritchard, B. P. Weiss, J. G. Williams, L. L. Hood, K. Righter, C. R. Neal, C. K. Shearer, I. S. McCallum, S. Tompkins, B. R. Hawke, C. Peterson, J. J. Gillis, and B. Bussey, 2006. Rev. Mineral. Geochem., 60, 221-364

Selenology Today

Wrinkle Ridges in Mare Nubium

By KC Pau Geologic Lunar Research (GLR) group

Wrinkle ridges are found almost in every lunar mare. They are formed when the lava cooled and contracted. Their features are in various forms, which is either straight, curved, or braided. Their width can be from a few meters to about 20 km and the height seldom exceeds 250 meters. Some ridges may stand alone or some may interconnect with other ridges to form a complex system. Wrinkle ridges are easily visible only when they are under oblique illumination and they cast spectacular shadows on the mare floor. They almost disappear when under high sun.

Most wrinkle ridges are found along the border of the lunar seas like those in Mare Crisium. Some may indicate the location of the basin inner ring like those in Mare Imbrium. Some may mark the crater wall of the submerged crater which is found in Mare Nubium. Among all the wrinkle-ridge systems on the near-side moon, those found in Mare Nubium are the most magnificent when under low angle sun illumination. There are at least 3 complex wrinkle ridge systems which are not assigned any name but they all seem to meet at the crater Nicollet. The interconnection among these systems form a spider web outline (Figs. 1-3).

East of Nicollet is a curved wrinkle ridge system. It probably marks the location of the western rim of a lava flooded ruin crater called “Ancient Thebit” by Dr. Charles Wood in his book “The Modern Moon”. This crater is about 200 km wide and its eastern rim is a well-defined mountain range with Thebit in the middle part (see Fig. 3). The Straight Wall stands along the center of the ruined crater.

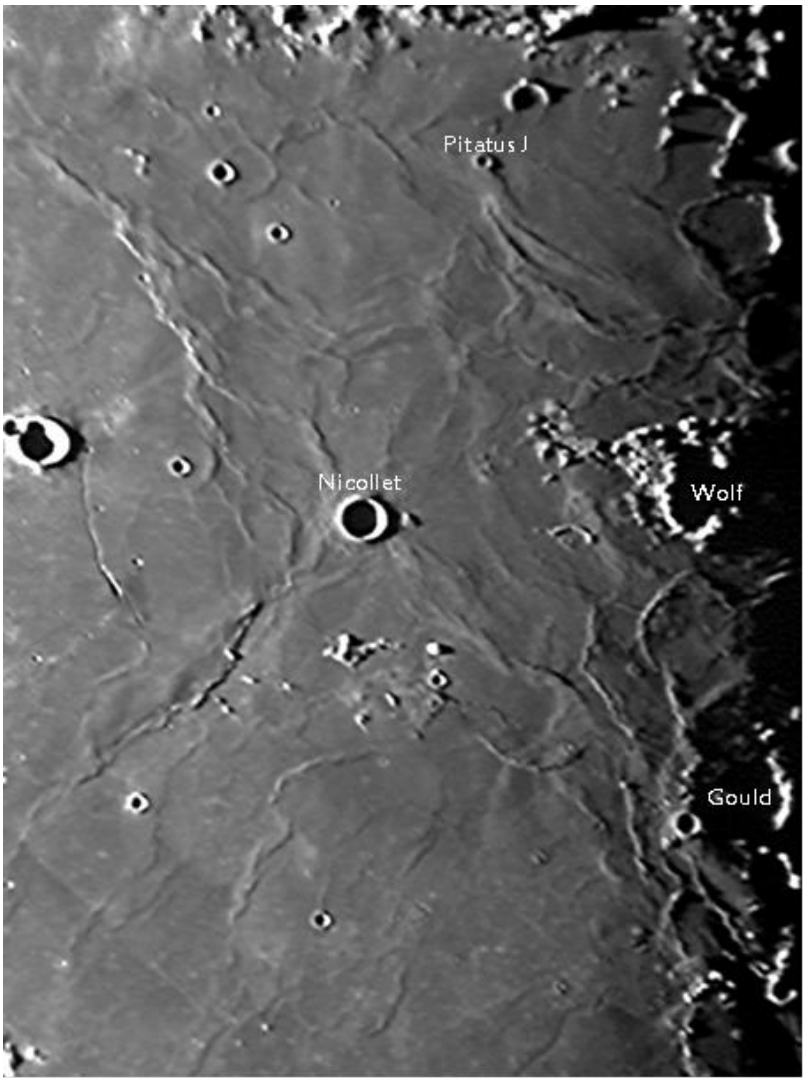

Fig. 1
Wrinkle ridge systems under the morning

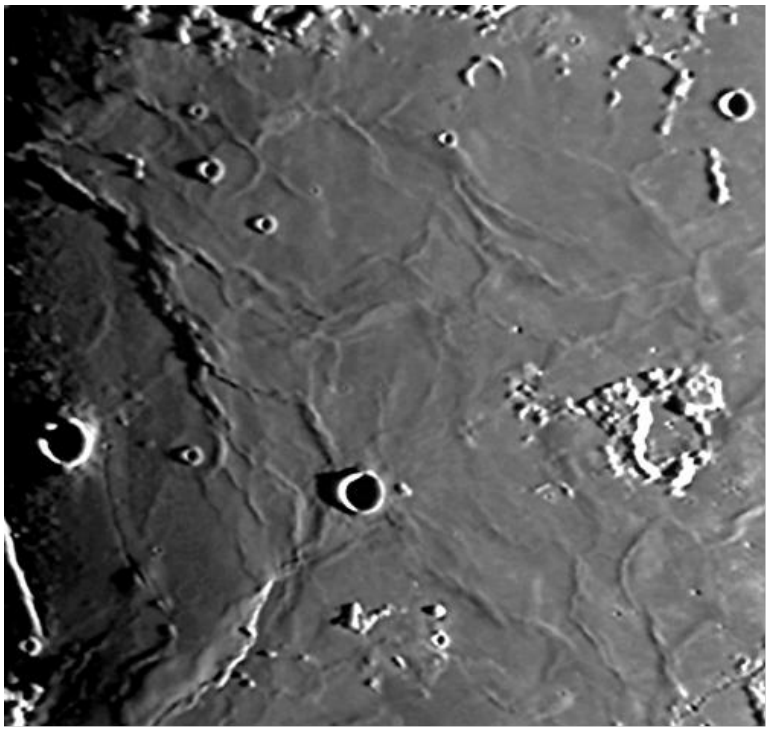

Fig. 2
Wrinkle ridge systems under the evening sunlight

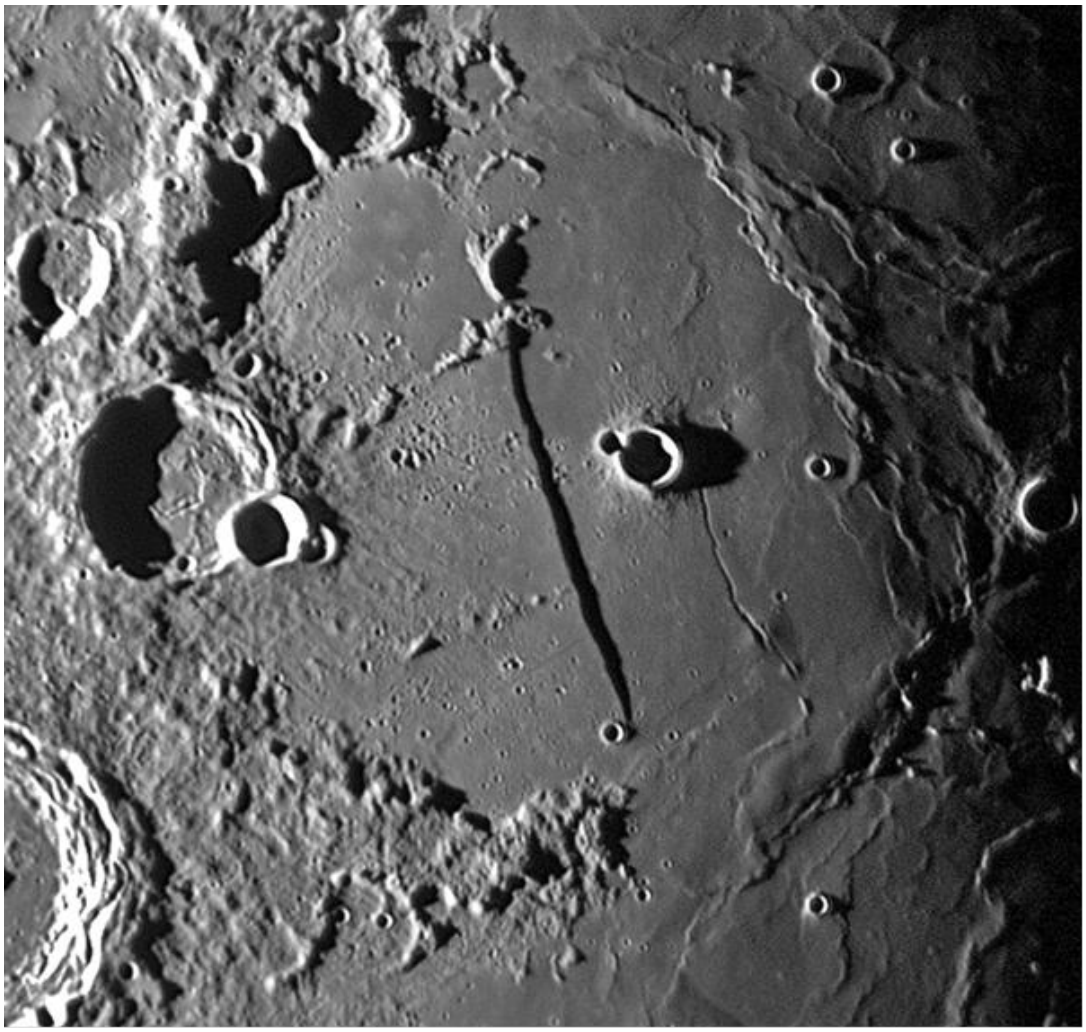

Fig. 3
Wrinkle ridge east of Nicollet

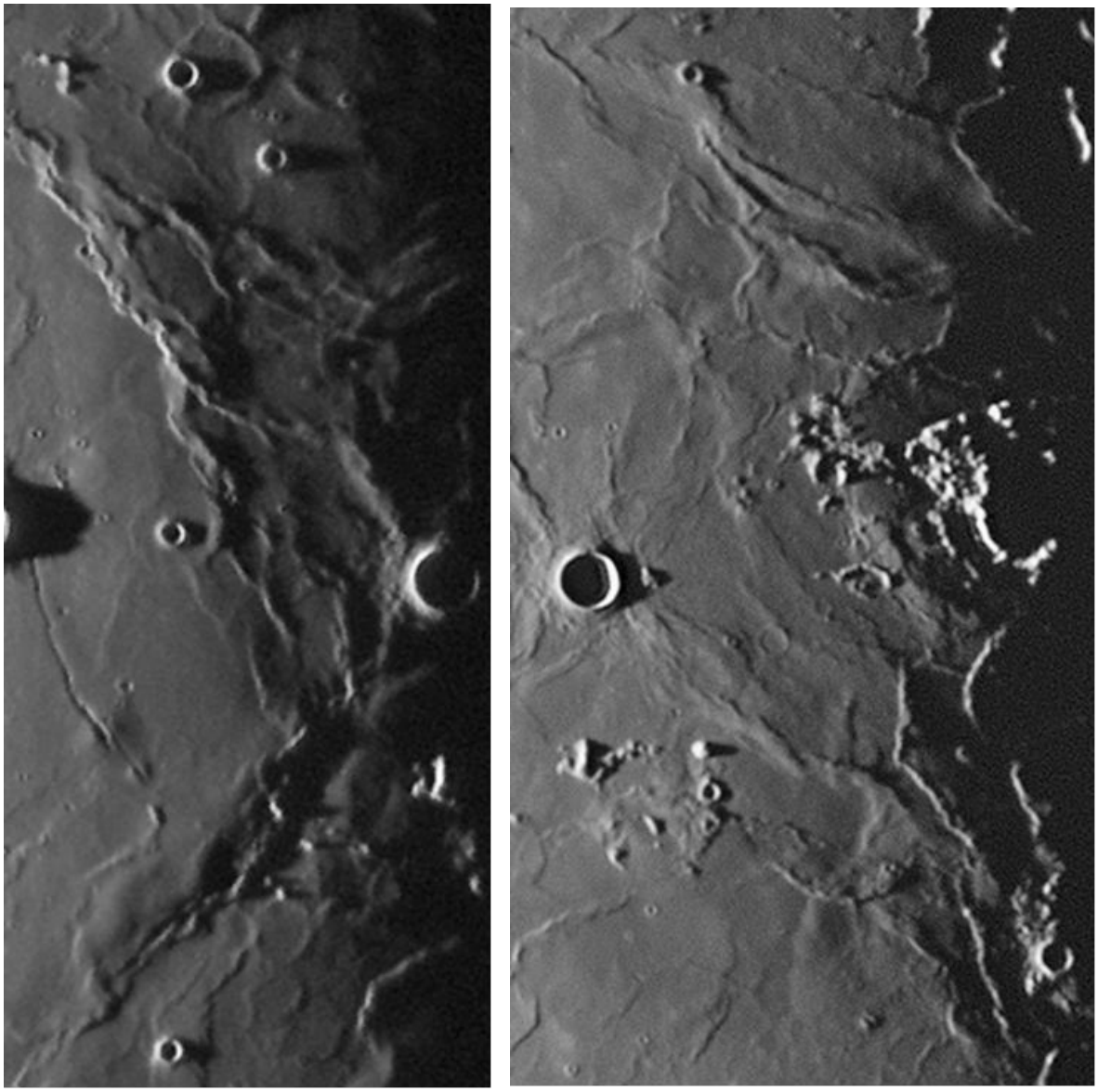

Fig. 4
Wrinkle ridge discussed in the text

This wrinkle ridge system is rather complex and is well-braided. It is best observed when Nicollet is near morning terminator. One of its tributary runs towards Nicollet. Another tributary intersect with another ridges arising east of small crater Pitatus J and form an ellipse lobe a distance south of Nicollet.

The ridge system arising from Pitatus J fans out towards craters Wolf and Nicollet. There is another ridge system arising from Nicollet and runs towards crater Gould (Fig. 4).

Fig. 4 left photo shows a close-up view of the complex wrinkle ridge system east of Nicollet. A few ghost craters are seen north of Nicollet. Fig. 4 right photo shows a close-up view of the wrinkle ridge system arising from Pitatus J, that fans out towards Nicollet and Wolf. Note the topography north-east of Wolf.

Reference

Wood, C., “The Modern Moon”. 2003, Sky Publishing

Selenology Today

3D reconstruction of the dome Yangel 1 obtained on ground-based high-resolution CCD imagery

By Raffaello Lena and Mike Wirths GLR group

Abstract

In this paper we examine the dome Yangel 1 (Ya1), associated with a lunar pyroclastic deposit (LPD), which was identified by Lena and Fitz-Gerald (2014) in a previous research.

Relying on ground-based high-resolution CCD imagery, we examine the morphometric characteristic of the Dome Ya1, making use of a combined photoclinometry and shape from shading technique. The results obtained with the described methodology are in excellent agreement with the measures obtained with the GLD100 dataset described in our published papers (Lena and Fitz-Gerald , 2014; Fitz-Gerald and Lena, 2014).

Using an image-based photoclinometry approach to reconstruct the three-dimensional shape of Ya1, we find that its height amounts to 620 ± 60 m, according with the previously results based on LRO WAC GLD100 dataset (Lena and Fitz-Gerald, 2014).

The LPD associated to the dome is an interesting target to be imaged by terrestrial CCD imagery. To our knowledge the described LPD identified by Lena and Fitz-Gerald (2014) has been not imaged from telescopic telescopes in high detail yet.

Introduction

The region surrounding the crater Manilius in Mare Vaporum is known for many lunar domes. In a previous article, Lena and Fitz-Gerald (Lena and Fitz-Gerald, 2014; Fitz-Gerald and Lena, 2014) have identified a previously unnoticed LPD and a dome, which was noticed but not interpreted as volcanic, located to the south of the entrance to Sinus Fidei (latitude 16.42° N and longitude 3.26° E).

The examined dome, termed Yangel 1 (Ya1), is located on the surface of the mare, and appears to overly the southern rim of a partially submerged pre-mare impact crater (Fig. 1). The size and geometry of this structure implies a construction composed of a combination of effusive lavas as well as pyroclastic deposits, though it is not possible to identify any individual lava flows, and the pyroclastic deposits appear to be very localised and limited in extent and form a veneer on the surface of the dome (Lena and Fitz-Gerald, 2014; Fitz-Gerald and Lena, 2014). This combination is novel and not seen in the data reported by Gustafson et al. (2012) and Gaddis et al. (2003) regarding previously cataloged LPDs (Fig. 2).

Based on the GLD100 dataset the dome Ya1 has a diameter of 5.2 km. Its height amounts to 620 m, while the average slope angle ξ corresponds to 13.4° and the edifice volume was estimated of about 5.3 km^3 (Lena and Fitz-Gerald, 2014).

The crater wall to the north is partially overlain by the northern slope of the steep dome, whilst the crater itself has its eastern wall breached by mare lavas which now occupy its floor. The crater rim to the west reaches a height of ~ 200 meters above the mare surface.

The fact that the examined dome Ya1 is steep sided is evidence that it is not just an accumulation of pyroclastic material but is an effusive viscous lava structure but different in composition to the highland domes characterized by more silicic composition and spectrally characterized by a low R_{415}/R_{750} ratio, appearing red in color ratio images of Clementine. The Selene-1 (Kaguya) color ratio image and Clementine UVVIS multispectral data indicate a higher titanium concentration for the dome and LPD which shows up bluer than the surrounding red mare

(Fig. 2).
In this paper our goal is to obtain a 3D reconstruction of the dome Ya1 by making use of a combined photoclinometry and shape from shading approach applied on a CCD terrestrial image. The results obtained are in excellent agreement with the GLD100 dataset.

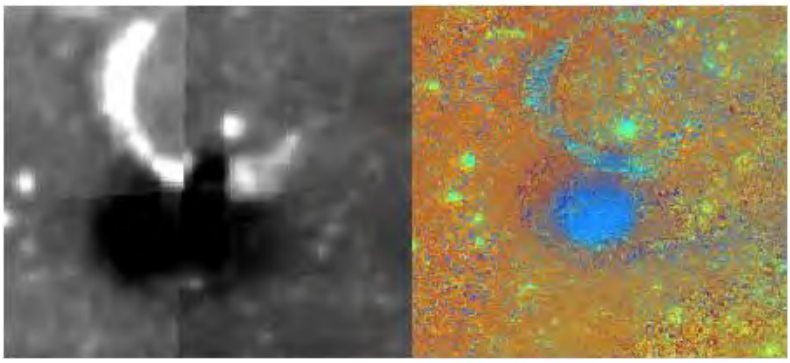

Figure 2.

(Left) Clementine 750 nm imagery of the Dome showing extent of LPD; (Right) Selene Ratio color image (R_{750}/R_{415} blue channel, $R_{75}0/R_{950}$ green channel and R_{415}/R_{750} red channel).

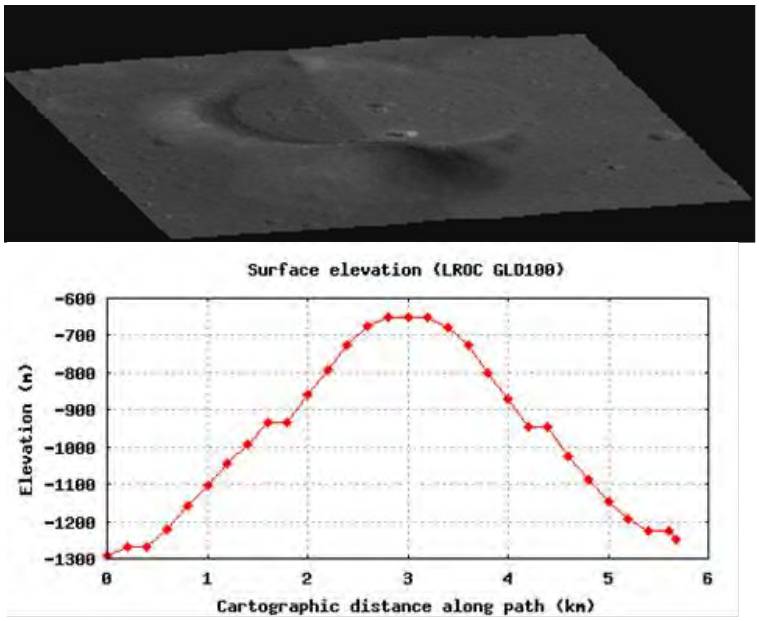

Figure 1.

LRO WAC-derived surface elevation plot of a west to east cross-section of Ya1 with its 3D reconstruction derived by elevation model GLD100 dataset, adopted by Lena and Fitz-Gerald (2014).

Telescopic CCD imagery

Fig. 3 display a CCD image of the examined region, taken with a Dobsonian telescope of apertures of 400 mm. The image was generated by stacking several hundreds of video frames, making use of the Registax software package. The scale of the images is 230 m per pixel on the lunar surface but the effective resolution due to atmospheric seeing, corresponding to the width of the point spread function, is typically not better than 1 km. The image was taken by Wirths on February 19, 2013 at 02:19 UT, using a Lumenera CCD camera. Using the LTVT software package by Mosher and Bondo (2006), we determined the selenographic positions, the solar altitude and the shadow length measurements. Image calibration was performed based on the UCLN 1994 list of control points.

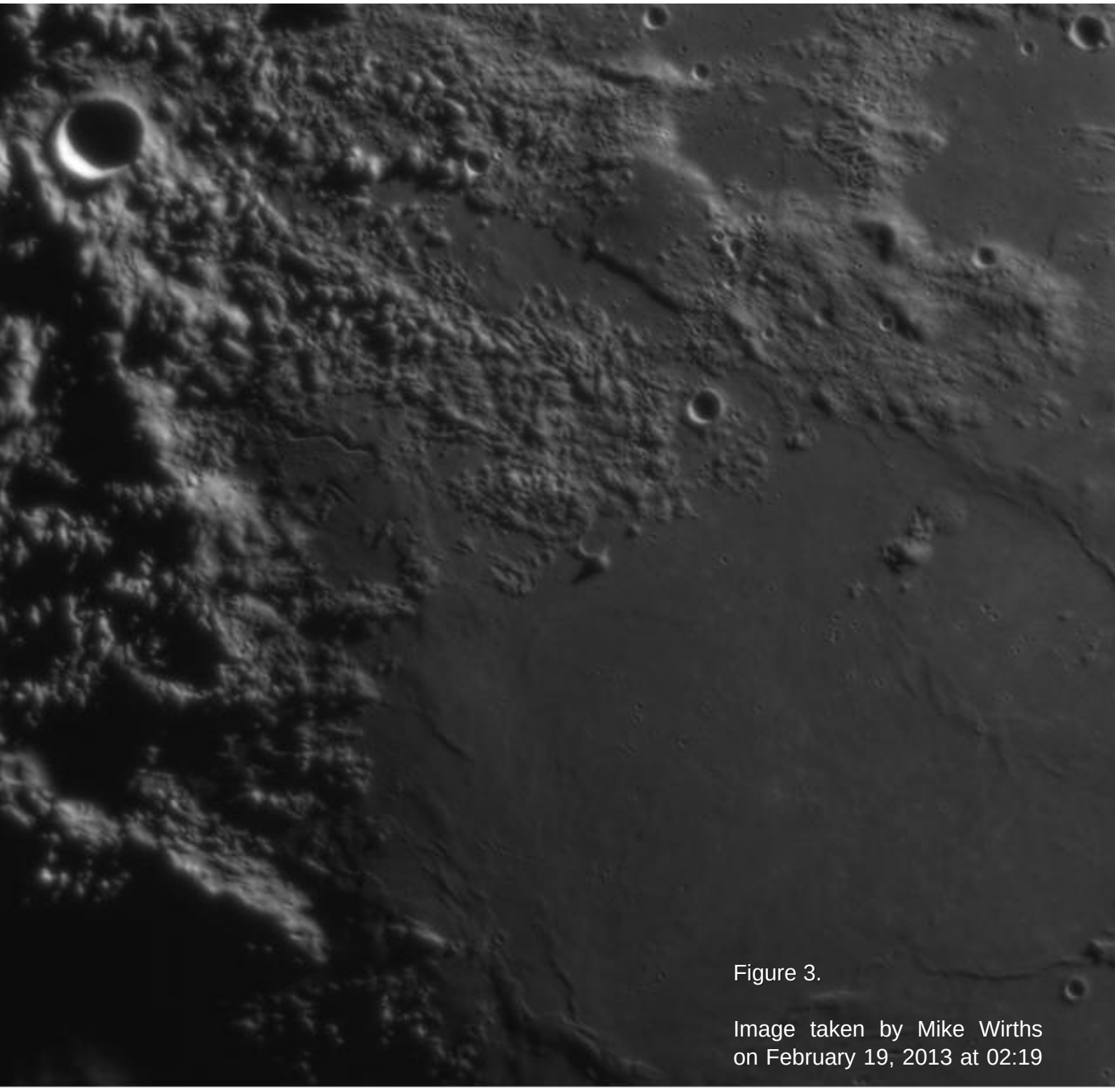

Figure 3.

Image taken by Mike Wirths on February 19, 2013 at 02:19

Shadow length measurement

A crop of the previous image displaying the steep dome is shown in Fig. 4, corresponding to a solar altitude over the examined lunar dome of 4.3°. Its height was computed by measuring the length of the shadow cast by its flank, which yield H= 621 ± 60 m, according with the preceding results obtained with the GLD100 dataset (Lena and Fitz-Gerald, 2014.
The slope ξ was computed using the equation

$$\xi = \arctan (2h/D),$$

where h and D denote the computed height and the diameter (D = 5.2 km in E-W direction).

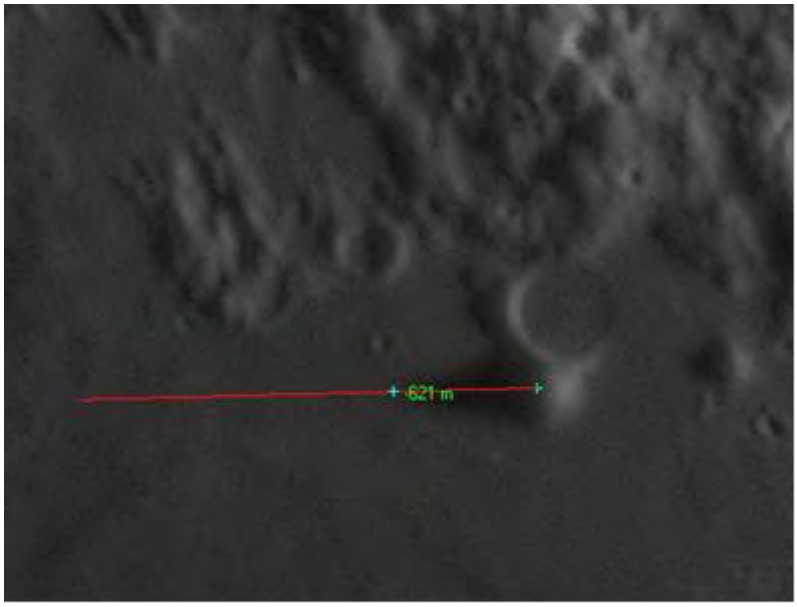

Figure 4.

Shadow length measurement carried out on the CCD terrestrial image.

3D reconstruction by making use of CCD terrestrial image

Generating an elevation map of a part of the lunar surface requires its three-dimensional (3D) reconstruction. We have also generated an elevation map of the dome based on our telescopic CCD image. A well-known image-based method for 3D surface reconstruction is shape from shading (SfS). The SfS approach aims for deriving the orientation of the surface at each image location by using a model of the reflectance properties of the surface and knowledge about the illumination conditions, finally leading to an elevation value for each image pixel (Horn, 1989). The iterative scheme used for photoclinometry and SfS approach is described in our preceding articles and it is not repeated here (cf. Lena et al., 2013; Wöhler et al., 2006; Wöhler et al., 2007; Lena et al., 2007). These techniques take into account the viewing direction of the camera, the illumination direction, and the surface normal in order to infer the pixel-wise surface normal and thus the three-dimensional shape of a surface section from the observed intensity distribution in the image. The dome height h is readily inferred from the resulting DEM, taking into account the effect of the curvature of the lunar surface, and corresponds to 620 ± 60 m resulting in an average flank slope of 13.4° ± 0.1°. The obtained 3D reconstructions are shown in Figs. 5 and 6.

Conclusion

The study of domes provides lunar observers with an opportunity for systematic observations of the Moon. Moreover, our Consolidated Lunar Dome Catalogue is continuously updated according to ongoing observing and modelling activities. In fact, our future target will be the publication of a Lunar dome atlas. In this work we have obtained a 3D reconstruction of the dome Ya1 by making use of a combined photoclinometry and shape from shading approach applied on a CCD terrestrial image. The result obtained is in excellent agreement with the GLD100 dataset.

To our knowledge the described LPD, identified by Lena and Fitz-Gerald (2014), has been not imaged from telescopic images in high detail yet. Hence, the LPD associated to the dome is (Fig. 2) a difficult but interesting target to be imaged by terrestrial CCD imagery. Any observations that readers can make about the eventual image of the LPD (with images taken under high solar illumination) will be gratefully received for our survey (contact Raffaello Lena: gibbidomine@libero.it).

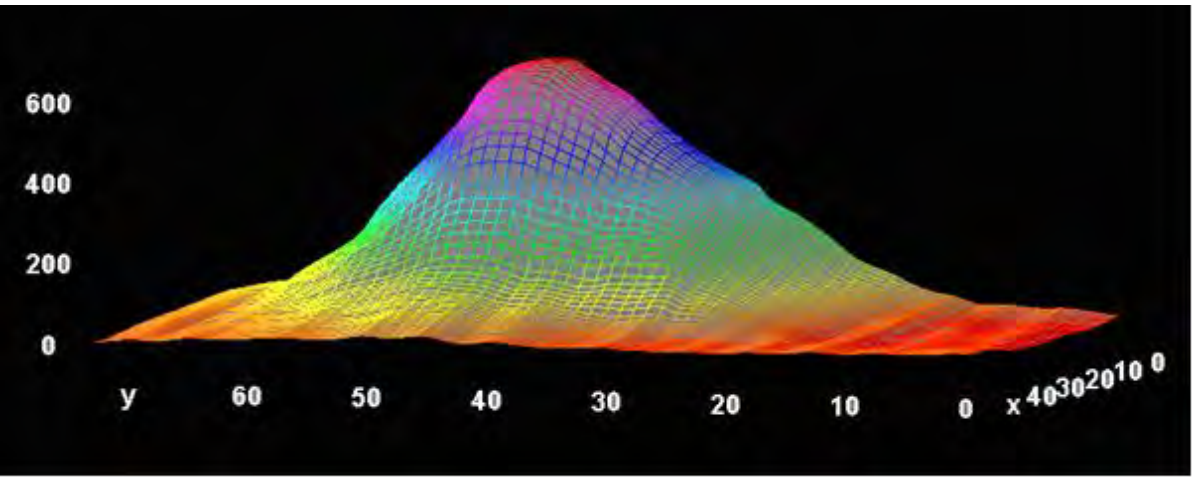

Figure 5.

3D reconstruction of Ya1 obtained by making use of the examined terrestrial image. The vertical axis is 10 times exaggerated.

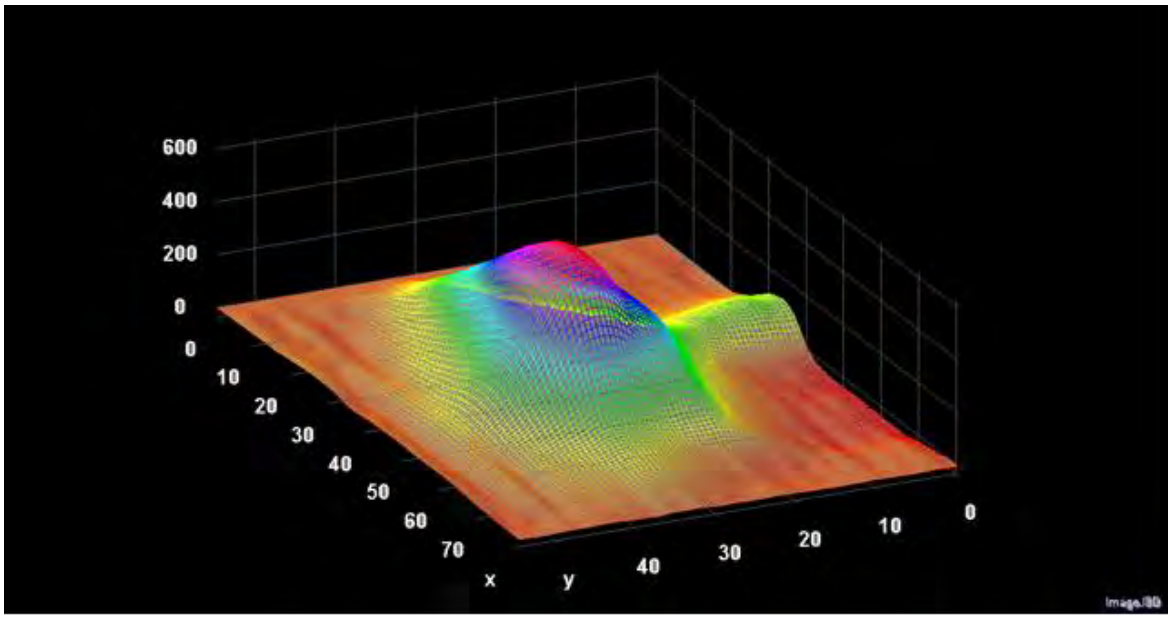

Figure 6.

3D reconstruction of Ya1 obtained by making use of the examined terrestrial image. The vertical axis is 10 times exaggerated. The reconstruction also displays the western crater rim 200 m high.

Appendix

A crop of another recent Yangel dome image made by Wirths on April 8, 2014 at 04:05 UT.
The LPD associated to the dome well detectable on probes imagery has been not imaged from telescopic images in high detail yet. Hence this is a future target for active lunar observers.

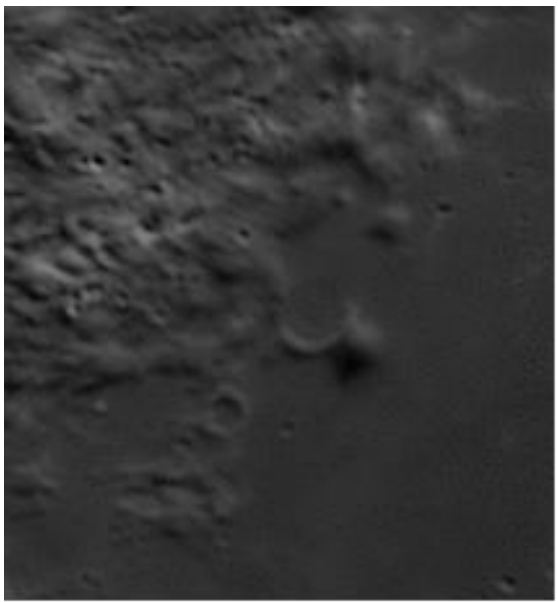

References

Gaddis, L.R., Staid, M.I., Tyburczy, J.A., Hawke, B.R., Petro, N.E.: Compositional analyses of lunar pyroclastic deposits. Icarus. 161, 262–280 (2003)

Gustafson, J. O., Bell III, J. F., Gaddis, L. R., Hawke, B. R., and Giguere, T. A.: Characterization of Previously Unidentified Lunar Pyroclastic Deposits using Lunar Reconnaissance Orbiter Camera Data, Journal of Geophysical Research, v. 117(E00H25), doi:10.1029/2011JE003893 (2012)

Fitz-Gerald, B., and Lena, R.: A Lunar Volcanic Dome and associated Pyroclastic deposits in Northern Mare Vaporum.Lunar and Planetary Science Conference XXXXV, abstract #1010, The Woodlands, Texas (2014)

Gustafson, J. O., Bell III, J. F., Gaddis, L. R., Hawke, B. R., and Giguere, T. A.: Characterization of Previously Unidentified Lunar Pyroclastic Deposits using Lunar Reconnaissance Orbiter Camera Data, Journal of Geophysical Research, v. 117(E00H25), doi:10.1029/2011JE003893 (2012)

Horn, B. K. P., 1989. Height and Gradient from Shading. MIT technical report 1105A. http://people.csail.mit.edu/people/bkph/AIM/AIM-1105A-TEX.pdf

Lena, R., Fitz-Gerald, B.: On a volcanic construct and a lunar pyroclastic deposit (LPD) in northern Mare Vaporum. Planetary and Space Science Volume 92, March 2014, Pages 1–15 (2014)

Lena, R., Wöhler, C., Phillips, J., Chiocchetta, M.T., 2013. Lunar domes: Properties and Formation Processes, Springer Praxis Books

Lena, R., Wöhler, C., Phillips, J., Wirths, M., Bregante, M.T.: Lunar domes in the Doppelmayer region: spectrophotometry, morphometry, rheology and eruption conditions. Planet. Space Sci. 55, 1201–1217 (2007)

Mosher, J., & Bondo, H., 2006. Lunar Terminator Visualization Tool (LTVT). http://inet.uni2.dk/ d120588/henrik/jim ltvt.html

Wöhler, C., Lena, R., Lazzarotti, P., Phillips, J., Wirths, M., Pujic, Z.: A combined spectrophotometric and morphometric study of the lunar mare dome fields near Cauchy, Arago, Hortensius, and Milichius. Icarus. 183(2), 237–264 (2006)

Wöhler, C., Lena, R., Phillips, J.: Formation of lunar mare domes along crustal fractures: rheologic conditions, dimensions of feeder dikes, and the role of magma evolution. Icarus. 189(2), 279–307 (2007)

Selenology Today

Report on the Total Lunar Eclipse of 2014 April 15

by Maurice Collins, Palmerston North, New Zealand.

The weather the previous day had be solid rain, and it was forecast to be raining at the time of the eclipse, even the local newspaper website warned people not to expect to see anything as rain was expected to pass over just at the time of the total lunar eclipse. However, lucky for this region of the country anyway, it was a nice fine day all day, and it stayed clear in the east for moonrise. The Moon could be seen partially obscured by the umbra as it rose above the hills and trees. Our view in that direction was blocked by trees and buildings, but my family and I - my wife was first to see it - could see it best from inside, as house is higher than the ground level.

I setup two telescopes and used binoculars to view the eclipse. I setup the ETX-90 in case I had to move around the yard a bit, and the Williams Optics FLT-110 f/7 refractor. As it turned out, where I setup the refractor was not a good location, so I ended up moving it after I had it all set to where I could see the Moon through a gap in the trees and between the buildings. It was back up against the bushes, but gave us a good view throughout the eclipse. My wife and daughter were very keen to get a look through the telescopes. They liked the view with the refractor best and when I compared the views I could see why. The view in totality through the 90mm telescope was so dim the Moon was hardly visible, and no colour was discernible by eye at the low light levels. So we gave up using that. Yet through the 110mm refractor it was bright, and orange coloured and background stars were very clearly visible (some showed up in the images also). We took photos afocally through various eyepieces and using a Fuji A800 8.3MP camera, and a mini iPad. The iPad ones were surprisingly good but was difficult to line up through the eyepiece to get the whole of the lunar disk. My wife (Dr Lesley Collins) took some images with the iPad, and I the remaining images with both cameras. I did try the ASI120MC imager on the Moon, but got nothing of value as the images were so dark, even increasing the exposure. Plus it hogged up the telescope for viewing so I abandoned it until later, where I took images of Mars during the eclipse after clouds started to suddenly move over from the western sky and my wife and daughter (Shannen) had gone inside. I did not attempt any timings of contacts with features, some could probably be worked out from the images, but that was not my purpose during this eclipse. The aim was to see it (a very lucky event as most of the country did not see it due to clouds) and to share it with my family. It is my daughter Shannen's first eclipse that she can remember (though she had seen others but too young at the time to remember them now). She found it interesting, but thought it would look more blood red than the dark orange it was.

The darkness of the totality was very dim. It is one of the darkest eclipses I can remember, and like I mentioned, the view through the 90mm telescope was almost nonexistent with a 25mm eyepiece (50x), it was just so dim, even while dark adapted. I had not seen that before in past eclipses. The view with the naked eye was a dark red/brown Moon hanging in the sky next to Mars. Very striking. On the Williams Optics refractor I started using the Celestron 25mm eyepiece (30.8x magnification), then switched to the University Optics 25mm that was in the ETX-90 (not being used at the time) as it gave an even better image. I then remembered that I had a Celestron 32mm eyepiece that I had bought in Singapore, so got that out and it gave the best brightest views of all at a low 24x magnification.

It also made it easier to shoot afocal images, especially with the iPad. As I mentioned, the eclipse seemed very dark, and other observers around the country concurred with that. On the Danjon scale, with the naked eye it would be L = 1, Dark Eclipse, gray or brownish colouration, details distinguishable only with difficulty. But photographically and telescopically, it would be L = 2 Deep red or rust-coloured eclipse. Very dark central shadow, while outer edge of umbra is relatively bright. So it depends on your optical aid. However it was one of the darkest I can recall seeing.

After mid-eclipse, I moved telescope to Mars and image it at 0803UT as clouds were rolling in. I only saw the Moon occasionally after that through gaps in the clouds. I packed up the telescope gear after about 0810UT and went inside. It was great the sky was clear for it, and good that it was also early enough in the evening to enjoy it with the family. The next lunar eclipse, in October, will be late, around midnight so will probably be a solo event.

The times for the lunar eclipse were (from time and date dot com website http://www.timeanddate.com/eclipse/lunar/2014-april-15):

Lunar eclipses look approximately the same all over the world and happen at the same time.
The times displayed might be a minute or two off actual times.

Event	UTC Time	Time in Palmerston North*	Visible in Palmerston North
Penumbral Eclipse begins	15 Apr at 4:55 a.m.	15 Apr at 4:55 p.m.	No, below horizon
Partial Eclipse begins	15 Apr at 5:59 a.m.	15 Apr at 5:59 p.m.	Yes
Full Eclipse begins	15 Apr at 7:08 a.m.	15 Apr at 7:08 p.m.	Yes
Maximum Eclipse	15 Apr at 7:46 a.m.	15 Apr at 7:46 p.m.	Yes
Full Eclipse ends	15 Apr at 8:23 a.m.	15 Apr at 8:23 p.m.	Yes
Partial Eclipse ends	15 Apr at 9:32 a.m.	15 Apr at 9:32 p.m.	Yes
Penumbral Eclipse ends	15 Apr at 10:36 a.m.	15 Apr at 10:36 p.m.	Yes

* The Moon is below the horizon in Palmerston North some of the time, so that part of the eclipse is not visible.

Eclipse at 0733UT

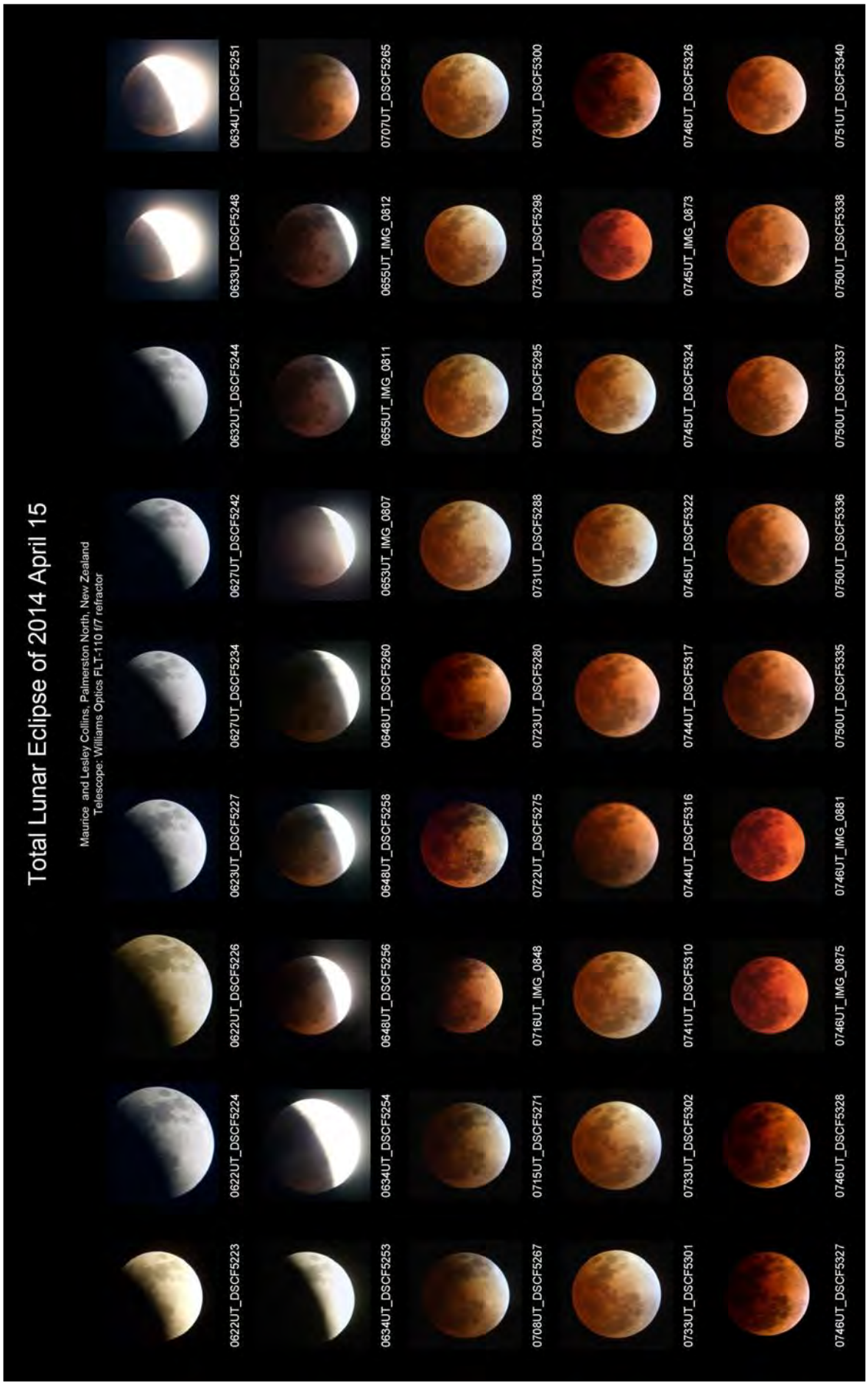
Total Lunar Eclipse of 2014 April 15
Maurice and Lesley Collins, Palmerston North, New Zealand
Telescope: Williams Optics FLT-110 f/7 refractor
0622UT_DSCF5223
0622UT_DSCF5224
0622UT_DSCF5226
0623UT_DSCF5227
0627UT_DSCF5234
0627UT_DSCF5242
0632UT_DSCF5244
0633UT_DSCF5248
0634UT_DSCF5251
0634UT_DSCF5253
0634UT_DSCF5254
0648UT_DSCF5256
0648UT_DSCF5258
0648UT_DSCF5260
0653UT_IMG_0807
0655UT_IMG_0811
0655UT_IMG_0812
0707UT_DSCF5265
0708UT_DSCF5267
0715UT_DSCF5271
0716UT_IMG_0848
0722UT_DSCF5275
0723UT_DSCF5280
0731UT_DSCF5288
0732UT_DSCF5295
0733UT_DSCF5298
0733UT_DSCF5300
0733UT_DSCF5301
0733UT_DSCF5302
0741UT_DSCF5310
0744UT_DSCF5316
0744UT_DSCF5317
0745UT_DSCF5322
0745UT_DSCF5324
0745UT_IMG_0873
0746UT_DSCF5326
0746UT_DSCF5327
0746UT_DSCF5328
0746UT_IMG_0875
0746UT_IMG_0881
0750UT_DSCF5335
0750UT_DSCF5336
0750UT_DSCF5337
0750UT_DSCF5338
0751UT_DSCF5340

Lunar Eclipse Images and reports

By Mike Wirths

I was visually looking at the eclipse in my 18" and a 24mm panoptic ep (the seeing was fairly poor). I also had a 20X90mm Oberwerk binocular setup on a tripod --it gave the best low power views.

My Wife Pamela was imaging with her Canon T4i and telephoto. I attached the best shot, using 800 ISO. I believe thats 76 Virginis and Spica off to the right of the moon.

By Maurice Collins

It turned out clear here in the Manawatu for the Lunar Eclipse right up to after mid-eclipse where some thin clouds appeared, but that was ok as got to see the best of it. It was very nice. I was only able to take snapshots, not having the right gear for whole moon images in one go. So not the best but all there is. Great to see it. It looked quite dark at times, to me anyway. Spent most of the time taking pot shots through the eyepiece and letting my wife do the same. We all had a good time looking at it too.

By Neal Simpson

It was taken in Nacogdoches, Texas. Equipment used was a Canon T4i (650D) DSLR with a Canon 50mm F1.8 lens on a fixed tripod.
This image is a composite of two photos. One short 1/5 second exposure for the moon and a longer 4 second exposure for the stars and pine trees (both F2.8, ISO 1600). The photos were processed in Adobe Lightroom and then combined in Paint.NET.

The total lunar eclipse at it's greatest. It came out much redder in the photo than it did with the naked eye. The star to in the lower right corner is Spica of the Virgo constellation.

Selenology Today

By Richard Hills

By Paul

Selenology Today

Selenology Today

Selenology Today